NUMERICAL SIMULATION & ANALYSIS OF ROOM TEMPERATURE PLASMONIC LASER

By

Md. Mesbahur Rahman

Student ID: S201206042

A thesis submitted in partial fulfillment of the requirements

for the degree of Bachelor of Science

in

the department of Electrical & Electronic Engineering,

Bangladesh University of Engineering & Technology, Dhaka

September 2017

CERTIFICATION OF APPROVAL

This is to certify that the work presented in the thesis is an outcome of the investigation carried out by the author, Md. Mesbahur Rahman under the supervision of Dr. Md. Zahurul Islam, Associate Professor, Department of Electrical & Electronic Engineering, BUET, Dhaka. It is declared that this thesis has been submitted only for the award of graduation.

_____

(Supervisor)
Dr. Md. Zahurul Islam
Associate Professor
Department of EEE
BUET

DECLARATION OF AUTHORSHIP

The author hereby declares that this thesis titled, “NUMERICAL SIMULATION & ANALYSIS OF ROOM TEMPERATURE PLASMONIC LASER” and the work presented in it are his own.

It is therefore confirmed that: Except where specific references are stated, the work embodied in this thesis paper is the outcome of result carried out by the author under the supervision of Dr. Md. Zahurul Islam, Associate Professor, Department of EEE, BUET.

This thesis has been submitted solely for the award of graduation. Neither the thesis nor any part of it has been submitted to or is being submitted elsewhere for any other purposes. Where any published works of others have been consulted, that is always clearly attributed.

Md. Mesbahur Rahman

September, 2017

TABLE OF CONTENTS

LIST OF FIGURES

ACKNOWLEDGEMENT

First, I would like to express my gratitude towards the Almighty Allah for whatever I have achieved thus far in my academic career. I am also thankful to him for enabling me to complete this thesis. I would like to take this opportunity to thank my parents for their love, guidance and support throughout my life.

Next, I would like to express gratitude towards my thesis supervisor, Dr. Md. Zahurul Islam for the patient guidance, advice and motivation that he has given throughout the time I have been his student. I consider myself extremely lucky to have such a wise, knowledgeable, and helpful supervisor who not only answered all the questions and queries and but also provided ample reading materials to aid my research endeavor. I will always be thankful to him for introducing me to the world of research and teaching a systematic approach towards research work.

I also would like to thank 'Robert Noyce lab, BUET' for permitting me to work with licensed version of MATLAB™ software.

ABSTRACT

In this work, we simulate two room temperature plasmonic lasers proposed by Ma et al [5] and Sidiropoulos et al [6]. Main obstacles towards the room temperature operation of plasmonic laser are electron high scattering and collision loss in metal in room temperature and radiation loss. Comparatively higher Q factor and cavity feedback are needed to overcome the metal loss for room temperature operation. In the two above mentioned plasmonic laser metal-insulator-semiconductor hybrid structures are used to increase optical confinement in the gap region for improvement of Q factor. The first structure improves the Q factor and cavity feedback further by employing total internal reflection of plasmonic mode in the device boundary and second structure improve them by matching the surface Plasmon frequency of the structure with emission frequency of the gain medium. Our simulation results also confirm the room temperature operation of those lasers. . In our simulation room temperature environment was modeled by using all the material refractive index and permittivity data of room temperature. Data required for modeling the gain medium i.e. the electron population density data were also used of room temperature to correctly model the room temperature conditions.

CHAPTER 1

Introduction

Communication plays a huge role in the modern era of science and technology. Mankind has always tied to achieve faster, cheaper and more effective ways of communication. Electronic and optical mean of communication have defined the 21st century. Electronic circuit components' size has reduced drastically over the past few decades. But due to some physical limitation transistors cannot be reduced than few nanometers. On the other hand optical devices can be very cheap, efficient and small in size.

Lasers are one of the most used optical devices in recent past for their fast, coherent and high intensity nature. Lasers have been the brightest source of high frequency electro-magnetic radiation with application spanning all physical science and engineering since the first demonstration over 50 years ago [1]. Over the past few decades laser science has seen tremendous development of high intensity lasers for nuclear fusion [2,3]. Faster laser for probing chemical reactions and smaller lasers for large scale in-tegrated optical data networks that form the backbone of the internet [4]. Laser technology has evolved from gas laser to semiconductor p-n junction lasers. After that , double heterostructure, quantum dot, quantum cascade lasers have been implemented [7]. Significant improvement in laser performance was brought about

through discovery of distributed feedback lasers, vertical cavity surface emitting lasers, photonic crystal lasers, and many other types of lasers [8]. The trend has always been to reduce the laser size. However , the dielectric semiconductor laser structure is limited by the diffraction limit of light which cannot be less than half of the wavelength in operation [9]. Recently, a new class of optical amplification and laser action was demonstrated for charge density waves at the nanoscale, named plasmon lasers or spaser [10-18]. In contrast to classical lasers, plasmon lasers amplify light coupled to oscillating electrons. This discoveries have opened a new possibility in the demonstration of nanolasers using metal-optics. In this work, two distinct structures of room temperature plasmonic laser have been simulated and explained which can operate beyond the diffraction limit of light.

1.1 Plasmonic Laser: State of The Art

Plasmonics in laser application is used for coupling photons in nanoscale dimensions. Surface plasmon polariton (SPP) modes propagate along a metal-dielectric interface typically at visible or infrared wavelengths. Many other forms of metal structures apart from flat metal-dielectric interface such as metallic nano-particles, grooves, holes, gaps, and slits on metal films can couple plasmonic mode. This plasmonic mode propagates via resonant energy transfer between electromagnetic wave and charge density wave in metal. Interaction with free electrons in metal causes plasmonic waves to dissipate energy which leads to exponential decaying along the propagation direction. This metallic loss is a fundamental property of plasmonic modes.

To achieve lasing emission from plasmonic structure, the gain medium has to overcome these metallic losses.

Limited only by a metal's in-homogeneity and non-locality length scale (1 nm) the minimum physical size of a plasmon laser can be just a few nanometers [19]. New features of plasmon laser are evident with unprecedented small physical size and mode volume. Firstly, by enhancing spontaneous emission the strong electromagnetic confinement in a plasmon cavity modifies the laser action [12, 14, 20–22]. This causes a drastic spatial redistribution of spontaneous emission. That is to say, light can be inhibited into some modes and preferentially coupled to the laser mode. This can significantly reduce the pump conditions for the onset of laser action and will modify the threshold behavior. Secondly, the electron collision time within metals is of the order of 100 femtoseconds, leading to the high Ohmic loss of the plasmon cavity. This can affect a number of processes within a laser, but most importantly, due to this short plasmon lifetime and the high Purcell factor, plasmon lasers can be potentially modulated at frequencies in the terahertz range [19, 23].

The recent emergence of plasmon lasers now stimulates the exploration of nanometer-scale science and application to-wards the rich physics of deep sub-wavelength optics and the development of high performance devices with sizes comparable to that of viruses (or a transistor inside a CPU) With the ability to generate high intensity electromagnetic radiation at the nanoscale in femtosecond timescales . For instance, enabling feature sizes beyond the limits of conventional lasers the highly focused near field of plasmon lasers could be used for photolithography [26].

Bergman and Stockman proposed in 2003 that a coherent light field can be generated directly at the nano-scale by lasing into localized surface plasmons [27]. Compared to photonic cavities this shows confinement of optical energy beyond the diffraction limit in a much more efficient and compact way. The first plasmon lasers were not experimentally presented until 2009 though several groups observed stimulated emission of surface Plasmon earlier than 2009 [28, 29],. Within three months of each other three groups reported plasmon lasers in three different configurations. Furthermore, each group demonstrated a plasmon laser exhibiting sub-wavelength confinement in a different number of dimensions. An elongated pillar structure defining two closely spaced metal walls sandwiching a gain medium was reported by Hill and co-workers [10]. By supporting a confined waveguide mode that overlaps with the III-V (InGaAs) gain media, this Metal-Insulator-Metal (MIM) waveguide-cavity provides plasmonic confinement in one dimension between the metal walls. The mode's reflections at the metal-coated waveguide end facets defined a Fabry-Perot cavity to provide feedback for the laser. Later, A hybrid nanowire Metal-Insulator-Semiconductor (MIS) plasmon laser was reported by Oulton et al. [12]. The MIS hybrid design achieves strong optical confinement in the insulating gap region (few nanometers thick) in two dimensions. The two end facets of the nanowire act as mirrors to form a Fabry-Perot cavity. A localized surface plasmon laser comprised of a dielectric clad spherical gold particle measuring just 44 nm in diameter was reported by Noginov and co-workers [11]. While a Silica shell impregnated with OG-488 dye molecules serves as the gain medium, the 15 nm diameter gold particle supports a dipole-like plasmonic cavity mode. The dipole-like nature of the

resonance provides plasmonic confinement in all three spatial dimensions. While, varying in confinement dimensionality, in all three cases the plasmonic laser modes cannot be efficiently excited by resonant coupling from the far-field; efficient excitation is only possible by laser action directly into the plasmonic modes. These plasmon lasers use the two types of surface plasmon cavity: propagating surface plasmon polaritons resonating between two mirrors and localized surface plasmon.

A number of prism and grating coupling based plasmonic laser and surface plasmon amplification structure is reported [30, 31]. Kretschmann structure comprising 39 nm and 67 nm thick silver films on BK7 prisms with the other silver surface being in contact with the gain medium was the first demonstrated SPP laser, lasing emission at optical wavelength. Rhodamine 101 and cresyl violet in ethanol solution was as the gain medium used in this device [32]. Similar structure, but with gain medium comprising a 10 μm thick layer of poly(methyl methacrylate) (PMMA) was also reported to produce visible light stimulated emission [33].

Few plasmonic lasers have been proposed in last few years which are based on extraordinary transmission of light operating in optical communication wavelength [34, 35]. In such structures, loss compensation is provided by semiconductor gain medium deposited on top of metallic hole array. Lasing emission at visible wavelength has also been reported using Ag metallic hole array and R101-PVA gain layer [36]. Apart from nanohole array, other kinds of plasmonic crystals have been reported to produce lasing emission. In 2013, Zhou et. al. reported room temperature surface normal lasing action in strongly coupled plasmonic nanocavity array due to excitation of band-edge lattice

plasmon modes [37]. Au nano-particle array surrounded by organic gain material (IR-140) produced lasing emission in near-IR regime. Similar structure using plasmonic bow-tie antenna was reported to produce lasing emission [38]. Off normal lasing emission from similar structure with plasmonic nanodome array has been studied as well [39]. Several structures such as MIM (Metal-Insulator-Metal) [10], Distributed Feedback cavity [40], Whispering Gallery Cavity [41] ensure feedback through one dimensional confinement. While other structure such as Hybrid MIS (Metal-Insulator-Semiconductor) nanowire structure [12] and gold nanoparticle structure [11] deploy two and three dimensional confinement.

1.2 Issues Regarding Practical Implementation of Plasmonic Laser

In recent years, many attempts have been made to implement plasmonic nanolaser as practically as possible. However, there are a number of aspects of plasmonic nanolaser research that needs to be addressed. A fundamental issue with plasmonic laser is the Ohmic loss associated with it. Q factor of the plasmonic nanocavity cannot reach very high values due to this loss,. As a result, spectral coherence of the lasing emission suffers and material supporting high gains to compensate these losses is required. Another issue for such lasers is the divergence of emission. In many applications, spatial coherence from laser emission is essential. However, when plasmonic modes couple to free space radiation, it shows significant divergence. Minimizing divergence of emission is another active research topic for such lasers. Most of demonstrations of plasmonic nanolaser mentioned in the preceding section involve optical pumping. There are relatively a few numbers of reports of electrically pumped surface plasmon laser. Optical pumping poses

the engineering challenge to include another light source to pump the laser for usual application in photonic integrated circuits and many other applications. Another major practical issue is the requirement of cryogenic temperature operation for its proper operation. Due to the high metal loss because of electron scattering and collision at higher temperature the operation of most of the plasmonic laser are limited to very low temperature.

In spite of the obstacles provided by the numerous challenges plasmonic lasers have shown tremendous possibility in usage as a coherent intense at nanoscale dimensions. Over the years, many of the above mentioned challenges have been tried to address by numerous researchers. In this thesis, we present our work regarding the simulation and theoretical explanation of two distinct approach of resolving the issue of room temperature operation of plasmonic laser.

1.3 Overview of Thesis

In the following chapter, brief overview of plasmonics is provided. Firstly, Drude model of metal is formulated which is essential for understanding of the existence of plasmonic modes. It is followed by discussions on surface plasmon polariton modes and localized surface plasmon modes. These modes are essential for operation of plasmonic crystal based nano-cavities employed in our proposed nanolaser design. We look into the dispersion and excitation methods of the surface plasmon polaritons.

In chapter 3 the fundamentals of the laser and plasmonic laser are discussed. Numerous way of improving quality factor and cavity feedback has been discussed. Also

different approaches of low loss plasmonic waveguide for laser application are also presented.

In chapter 4, discussions on numerical techniques utilized in this work are presented. The numerical simulator used in this work is based on finite difference time domain (FDTD) method. The numerical model used for modeling the laser gain medium is also presented.

In chapter 5, the two simulation setups and settings of the two structures are presented. Different issues regarding the simulation are also addressed. The results of the simulation are also presented in this chapter. Theoretical backgrounds and explanations of the results are also covered in this chapter.

In chapter 6, we present our conclusions of this work on room temperature plasmonic nanolaser simulation. Scopes of future works and possible next approaches towards further improvement of the performance of the room temperature plasmonic laser are also presented.

1.4 Summary

In this chapter we reviewed the prospect of plasmonics in usage as coherent, intense light source that is laser. We also discussed some of the recent intervention of plasmonic laser. Lastly, some of the major issues related with practical implementation are discussed.

CHAPTER 2

Plasmonics

Plasmonics forms a major part of the fascinating field of nano-photonics, which explores how electromagnetic fields can be confined over dimensions on the order of or smaller than the wavelength. It is based on interaction processes between electromagnetic radiation and conduction electrons at metallic interfaces or in small metallic nanostructures, leading to an enhanced optical near field of sub-wavelength dimension. Free electron gas of metals exhibit macroscopic oscillation under proper excitation. The quantized oscillation of free electron plasma is called plasmon. Two modes of plasmon are Surface plasmon polariton and localized surface plasmon both of which have numerous applications in nano-photonics. In this section fundamentals of plasmonics are discussed with proper mathematics and physics.

2.1 Drude Model for Metal

Plasma state refers to a neutral gas of heavy ions and light electrons. Metals and heavily doped semiconductors can be treated as plasmas because they contain equal numbers of fixed positive ions and free electrons. The free electrons experience no restoring forces when they interact with electromagnetic waves. This contrasts with bound electrons that have natural resonant frequencies in the visible or ultraviolet. Over a

wide frequency range, the optical properties of metals can be explained by a plasma model, where a gas of free electrons of number density n moves against a fixed background of positive ion cores. For alkali metals, this range extends up to the ultraviolet, while for noble metals interband transitions occur at visible frequencies, limiting the validity of this approach. In the plasma model, details of the lattice potential and electron-electron interactions are not taken into account. Instead, one simply assumes that some aspects of the band structure are incorporated into the effective optical mass m of each electron. The electrons oscillate in response to the applied electromagnetic field, and their motion is damped via collisions occurring with a characteristic collision frequency $\gamma = 1/\tau$. τ is known as the relaxation time of the free electron gas.

$$m\ddot{\boldsymbol{x}} + m\gamma\dot{\boldsymbol{x}} = -e\boldsymbol{E} \tag{2.1}$$

Here, ω is the frequency of light. The first term represents the acceleration of the electron, while the second is the frictional damping force of the medium. The term on the right hand side is the driving force exerted by the light. Solving this equation, we can get the displacement, x(t). This displacement is related to polarization P of metal. Moreover, as we know from the definition of electric displacement, $D = \varepsilon_r\varepsilon_0E = \varepsilon_0E + P$. Here, ε_r is the relative permittivity of metal. From equation (2.1) the relative permittivity of the metal is obtained as,

$$\varepsilon_r = 1 - \frac{\omega_p^2}{\omega^2 + j\gamma\omega} \tag{2.2}$$

Where,

$$\omega_p^2 = \frac{Ne^2}{\varepsilon_0^2 m_0} \qquad (2.3)$$

Here, ε_r can be assumed for lightly damped system as to be,

$$\boldsymbol{\varepsilon_r = 1 - \frac{\omega_p^2}{\omega^2}} \qquad \textbf{(2.4)}$$

The dielectric function of the free electron gas (2.2) is also known as the Drude model of the optical response of metals. Drude model is essential for understanding the mechanism of surface plasmon polariton and localized surface plasmon modes. However, it is important to keep in mind that its 0accuracy is much better in the infrared regime compared to that in the visible range. The reason is that the Drude model only accounts for the contribution of the free electrons in the conduction band. When the frequency increases, multiple new absorption channel opens up which results in significant deviation from Drude model. For practical purposes, a big advantage of the Drude model is that it can easily be incorporated into time-domain based numerical solvers for Maxwell's equations, such as the finite-difference time-domain (FDTD) scheme [42]. Nevertheless, Drude model is sufficient for discussion of dispersion of surface plasmon modes to be discussed in the next section.

2.2 Surface Plasmon Polariton

Surface plasmon polaritons are electromagnetic excitations propagating at the interface between a dielectric and a conductor, evanescently confined in the perpendicular direction. These electromagnetic surface waves arise via the coupling of the electromagnetic fields to oscillations of the conductor's electron plasma. By altering the structure of a metal's surface, the properties of surface plasmons in particular their interaction with light can be tailored, which offers the potential for developing new types of photonic device. This could lead to miniaturized photonic circuits with length scales that are much smaller than those currently achieved. Surface plasmons are being explored for their potential in sub-wavelength optics, data storage, light generation, microscopy and bio-photonics.

2.2.1 SPP at Singular Metal-Insulator Interface

Fig. 2.1 shows the propagation geometry with a Air/Metal interface. For simplicity we are assuming a one dimensional problem, i.e., ε depends only on one spatial coordinate. Specifically, the waves propagate along the x-direction of a Cartesian coordinate system, and show no spatial variation in the perpendicular, in-plane y direction; therefore, $\varepsilon = \varepsilon(z)$. In all generality, assuming harmonic time dependence, $\mathbf{E}(\mathbf{r},t) = \mathbf{E}(\mathbf{r})\exp(-j\omega t)$ of the electric field, we can write Helmholtz equation given by,

$$\nabla^2 \boldsymbol{E} + k_0^2 \boldsymbol{\varepsilon} \boldsymbol{E} = 0 \tag{2.5}$$

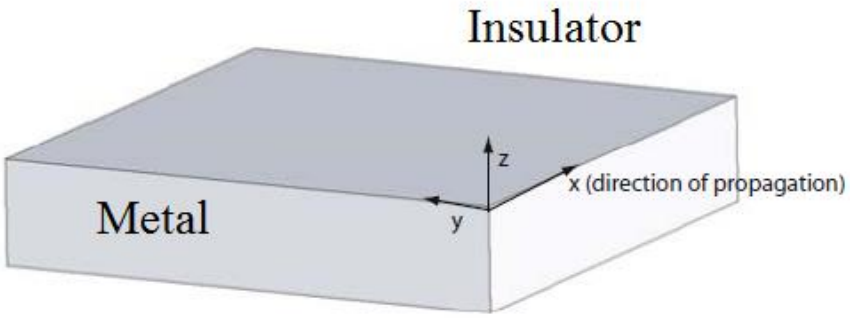

Figure 2.1: Definition of a planar wave geometry. The wave propagate along the x direction in a Cartesian coordinate system [43].

Here, $k_0 = \omega/c$ is the wave vector of propagating wave in vacuum.

For electromagnetic wave propagating in x direction, $\mathbf{E}(x,y,z) = \mathbf{E}(z)\exp(j\beta x)$. Here, complex parameter $\beta = k_x$ is called the propagation constant of the traveling wave and corresponds to the component of wave vector in the direction of propagation. Inserting this expression into Equation (2.5) gives,

$$\frac{\partial^2 \boldsymbol{E}}{\partial z^2} + (\boldsymbol{k}_0^2 \varepsilon - \beta^2)\boldsymbol{E} = 0 \qquad \textbf{(2.6)}$$

Similarly, The wave equation for TM mode is,

$$\frac{\partial^2 H_y}{\partial z^2} + (\boldsymbol{k}_0^2 \varepsilon - \beta^2)H_y = 0 \qquad \textbf{(2.7)}$$

The most simple geometry sustaining SPPs is that of a single, flat interface (Fig. 2.2) between a dielectric, non-absorbing half space (z >0) with positive real dielectric constant ε_2 and an adjacent conducting half space (z <0) described via a dielectric function $\varepsilon_1(\omega)$. The requirement of metallic character implies that $\mathrm{Re}[\varepsilon_1] < 0$. As shown in

chapter 1, for metals this condition is fulfilled at frequencies below the bulk plasmon frequency ω_p. We obtain a system of equations for each of the orthogonal directions. This system allows two sets of self-consistent solutions with different polarization properties of the propagating waves. We want to look for propagating wave solutions confined to the interface, i.e. with evanescent decay in the perpendicular z-direction.

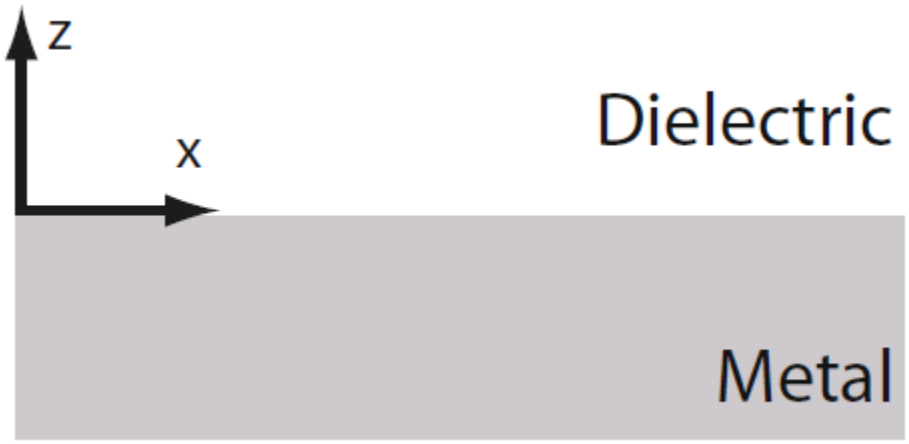

Figure 2.2: Geometry for SPP propagation at a single interface between a metal and a dielectric[43].

The TM solution of the system is given below, for z>0,

$$H_y(z) = A_2 e^{j\beta x} e^{-k_2 z} \tag{2.8}$$

$$E_x(z) = jA_2 \frac{1}{\omega \varepsilon_0 \varepsilon_2} k_2 e^{j\beta x} e^{-k_2 z} \tag{2.9}$$

$$E_z(z) = -A_1 \frac{\beta}{\omega \varepsilon_0 \varepsilon_2} e^{j\beta x} e^{-k_2 z} \tag{2.10}$$

For, z<0,

$$H_y(z) = A_1 e^{j\beta x} e^{k_1 z} \quad \textbf{(2.11)}$$

$$E_x(z) = -jA_1 \frac{1}{\omega \varepsilon_0 \varepsilon_2} k_1 e^{j\beta x} e^{k_1 z} \quad \textbf{(2.12)}$$

$$E_z(z) = -A_1 \frac{\beta}{\omega \varepsilon_0 \varepsilon_2} e^{j\beta x} e^{k_1 z} \quad \textbf{(2.13)}$$

Here, ki ≡ kz,i(i = 1,2) is the component of the wave vector perpendicular to the interface in the two media. Its reciprocal value, δz= 1/|kz|, defines the evanescent decay length of the fields perpendicular to the interface which quantifies the confinement of the wave. i.e. 1/|k2| is the evanescent decay length in the dielectric medium[43].

Figure 2.3(a) shows that surface plasmons at the interface between a metal and a dielectric material have a combined electromagnetic wave and surface charge character. They are transverse magnetic, TM in nature(H is in the y direction), and the generation of surface charge requires an electric field normal to the surface. This combined character also lead to the field component perpendicular (E_z) to the surface being enhanced near the surface and decaying exponentially with distance away from it. Figure 2.3(b) shows the evanescent field, reflecting the bound non-radiative nature of surface plasmons and prevents power from propagating away from the surface. In the dielectric medium above the metal the decay length of the field, δ_d, is od the order of half the wavelength of the light involved, whereas the decay length into the metal, δ_m, is determined by the skin depth.

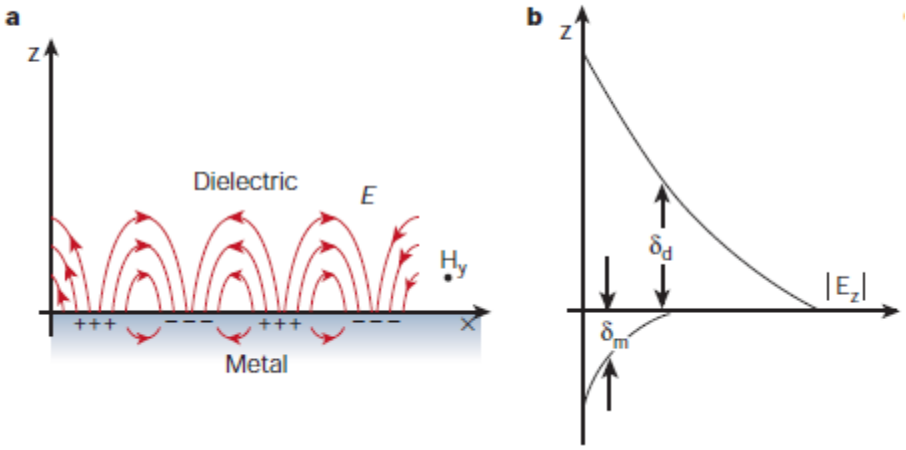

Figure 2.3: (a) Surface plasmons at the interface between a metal and dielcric. (b) The evanescent field [44].

Continuity of H_y and $\varepsilon_i E_z$ at the interface requires that $A_1 = A_2$ and and

$$\frac{k_2}{k_1} = -\frac{\varepsilon_2}{\varepsilon_1} \tag{2.14}$$

With our convention of the signs in the exponents in (2.8-10, 2.11-13) , confinement to the surface demands $Re[\varepsilon_1] < 0$ if $\varepsilon_2 > 0$ - the surface waves exist only at interfaces between materials with opposite signs of the real part of their dielectric permittivities, i.e. between a conductor and an insulator. Similarly, proper mathematical analysis show that no surface modes exist for TE polarization. Surface Plasmon polaritons only exist for TM polarization.

Putting the H_y into the wave equation 2.7 for TM mode we get,

$$k_1^2 = \beta^2 - k_0^2 \varepsilon_1 \tag{2.15}$$

$$k_2^2 = \beta^2 - k_0^2 \varepsilon_2 \tag{2.16}$$

Combining equation 2.14, 2.15 and 2.16 we obtain the center result of this section, the dispersion relation of SPPs propagating at the interface the two half spaces as,

$$\beta = k_0 \sqrt{\frac{\varepsilon_1 \varepsilon_2}{\varepsilon_1 + \varepsilon_2}} \qquad \textbf{(2.17)}$$

From the expression of E_z in TM mode solution it can be seen that for greater amount of confinement the values of k_1, k_2 and β should be large and β should be greater than k_0, the wave-vector of the corresponding electromagnetic wave in free space.

Figure 2.4 shows dispersion relation, the plots of equation 2.17 for a metal with negligible damping described by the real Drude dielectric function (equation 2.4) for an air ($\varepsilon_2 = 1$) and a fused silica ($\varepsilon_2 = 2.25$) interface. In this plot, the frequency ω is normalized to the plasma frequency ω_p, and both the real (continuous curves) and the imaginary part (broken curves) of the wave vector β are shown. Due to their bound nature that is for confinement requirement β to be greater than k_0, the SPP excitations correspond to the part of the dispersion curves lying to the right of the respective light lines of air and silica. Radiation into the metal occurs in the transparency regime $\omega > \omega_p$ (the continuous line in the upper left corner). Between the regime of the bound and radiative modes, a frequency gap region with purely imaginary β prohibiting propagation exists.

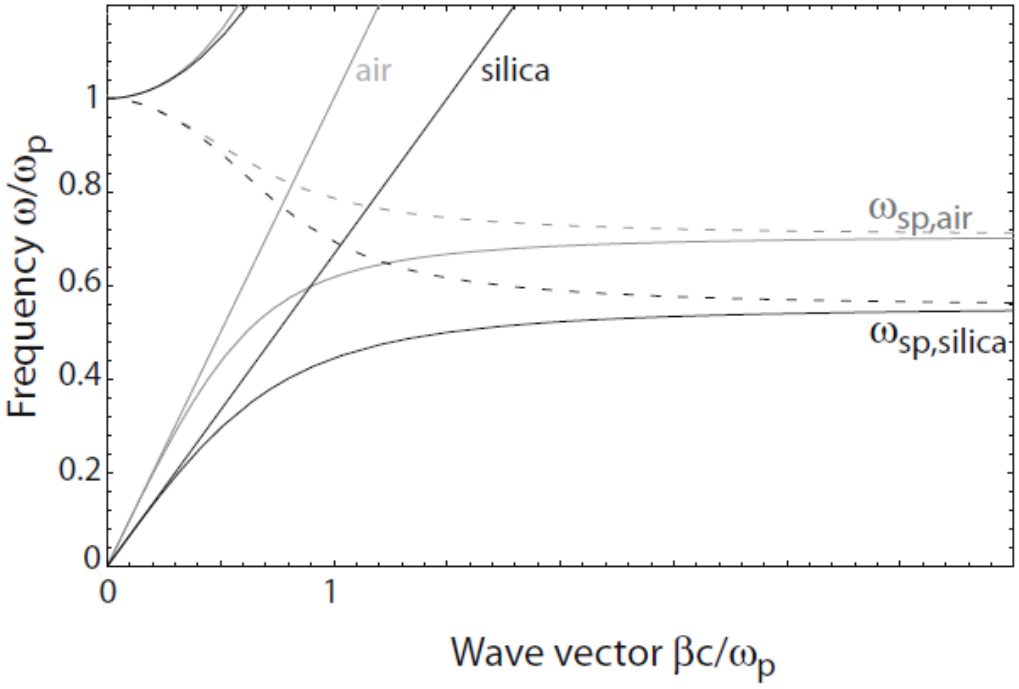

Figure 2.4: Dispersion relation of SPPs at the interface between a Drude metal with negligible collision frequency and air (gray curves) and silica (black curves) [43].

For small wave vectors corresponding to low (mid-infrared or lower) frequencies, the SPP propagation constant is close to k_0 at the light line, and the waves extend over many wavelengths into the dielectric space. In the opposite regime of large wave vectors, the frequency of the SPPs approaches the characteristic surface plasmon frequency as found by inserting the free electron dielectric function (equation 2.2) into equation 2.17,

$$\omega_{sp} = \frac{\omega_p}{\sqrt{1+\varepsilon_2}} \tag{2.18}$$

In the limit of negligible damping of the conduction electron oscillation (implying Im $[\varepsilon_1(\omega)] = 0$), the wave vector β goes to infinity as the frequency approaches ω_{sp}, and the

group velocity $v_g \rightarrow 0$. The mode thus acquires electrostatic character, and is known as the surface plasmon. For a metal with negligible damping described by a dielectric function of the form (2.4), this condition is fulfilled at ω_{sp}.

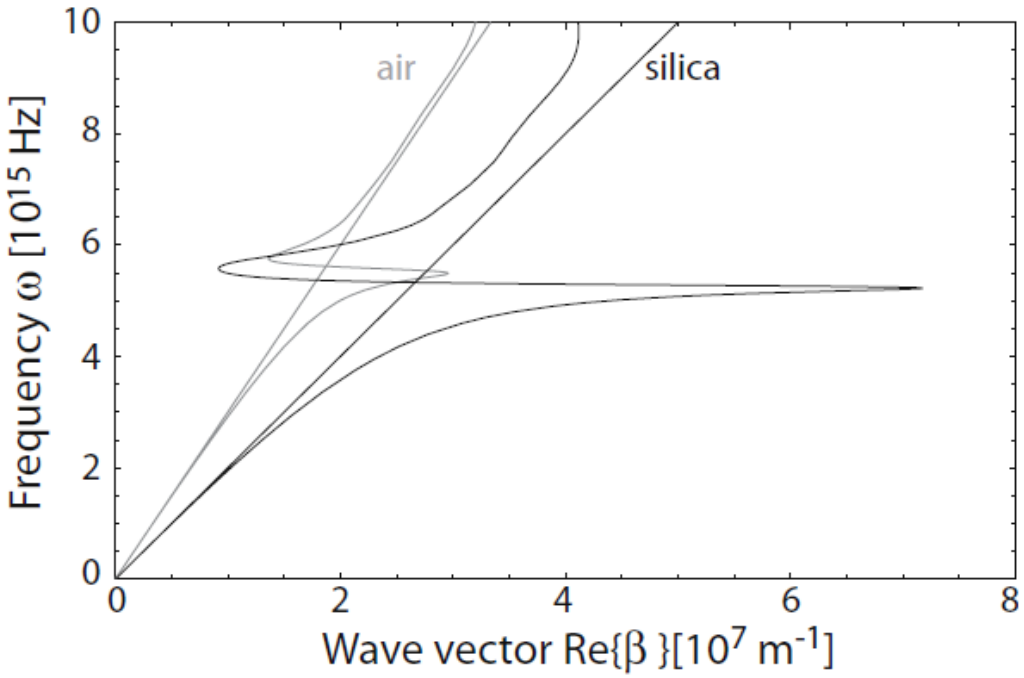

Figure 2.5: Dispersion relation of SPPs at a silver/air (gray curve) and silver/silica (black curve) interface. Due to the damping, the wave vector of the bound SPPs approaches a finite limit at the surface plasmon frequency [43].

However, excitations of the conduction electrons of real metals suffer both from free-electron and interband damping. Therefore, $\varepsilon_1(\omega)$ is complex, and with it also the SPP propagation constant β. The traveling SPPs are damped with an energy attenuation length (also called propagation length) $\delta_{sp} = (2\mathrm{Im}[\beta])^{-1}$, typically between 10 and 100 μm in the visible regime, depending upon the metal/dielectric configuration in question. Fig. 2.5 shows as an example the dispersion relation of SPPs propagating at a silver/air and

silver/silica interface, with the dielectric function $\varepsilon_1(\omega)$ of silver taken from the data obtained by Johnson and Christy [45]. Compared with the dispersion relation of completely undamped SPPs depicted in Fig. 2.4, it can be seen that the bound SPPs approach now a maximum, *finite* wave vector at the surface plasmon frequency ω_{sp} of the system. This limitation puts a lower bound both on the wavelength, $\lambda_{sp}= 2\pi/\mathrm{Re}[\beta]$ of the surface plasmon and also on the amount of mode confinement perpendicular to the interface, since the SPP fields in the dielectric fall off as $e^{-|k_z||z|}$ with $k_z=\sqrt{\beta^2 - \varepsilon_2(\frac{\omega}{c})^2}$. Also, the *quasibound*, leaky part of the dispersion relation between ω_{sp} and ω_p is now allowed, in contrast to the case of an ideal conductor, where $\mathrm{Re}[\beta]=0$ in this regime (Figure 2.4).

Both the propagation length, δ_{sp} and the energy confinement (quantified by δ_d) in the dielectric show a strong a strong dependence on frequency. SPPs at frequencies close to ω_{sp} exhibit large field confinement to the interface and a subsequent small propagation distance due to increased damping. The better the confinement, the lower is the propagation length. This characteristic trade-off between localization and loss is typical for plasmonics. We note that field confinement below the diffraction limit of half the wavelength in the dielectric can be achieved close to ω_{sp}.

2.3 Localized Surface Plasmon

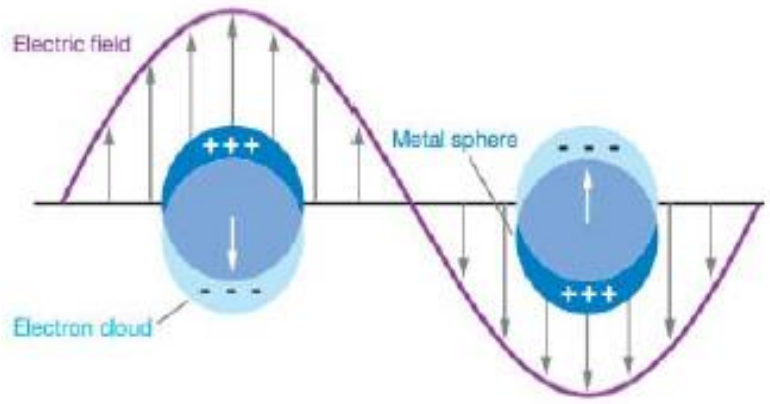

Figure 2.6: Dipolar localized surface plasmon supported by spherical metal particle [46].

The oscillation of the surface charge density in metallic nano-particles, commonly named localized surface plasmons (LSPs), is a result of the collective oscillation of the conduction electrons under the constraints imposed by the physical boundaries of the nano-particle geometry. The optical properties of metallic nanoparticles are determined by the excitation of electromagnetic surface modes. Localized plasmon modes are stationary oscillations of the surface charge density at optical frequencies along the metal boundaries of a metallic particle. The ability to control its resonance makes LSP modes makes LSP suitable in a number of applications such as photovoltaics, biosensing, spectroscopy, molecular fluorescence, etc [47, 48, 49].

2.4 Excitation of Surface Plasmon Polaritons at Planar Interface

Excitation by three-dimensional light beams is not possible unless special techniques for phase-matching are employed. Alternatively, thin film geometries such as

insulator-metal-insulator heterostructures sustaining weakly confined SPPs are amenable to end-fire coupling, relying on spatial mode-matching rather than phase-matching. Numerous excitation technique such as **Charged particle impact**, **Prism coupling**, **Grating Coupling**, **Highly focused optical beam** are available for surface plasmons excitation. Wave vectors in excess of $|\mathbf{k}|$ can also be achieved using illumination in the near-field, making use of evanescent waves in the immediate vicinity of a sub-wavelength aperture. For our simulation purpose, Highly focused optical beam method is used which is presented below.

2.4.1 Excitation Using Highly Focused Optical Beam

As a variant of the traditional prism coupling technique a microscope objective of high numerical aperture can be used for SPP excitation. Fig 2.7 shows a typical setup [50]. An oil-immersion objective is brought into contact with the glass substrate (of refractive index n) of a thin metal film via a layer of index-matched immersion oil. The high numerical aperture of the objective ensures a large angular spread of the focused excitation beam, including angles $\theta > \theta_c$ greater than the critical angle of total internal reflection at a glass/air interface. This way, wave vectors $k_x = \beta$ are available for phase-matching to SPPs at the metal/air interface at the corresponding angle $\theta_{SPP} = \arcsin(\beta/nk_0) > \theta_c$. Off-axis entrance of the excitation beam into the objective can further ensure an intensity distribution preferentially around θ_{SPP}, thus reducing the amount of directly transmitted and reflected light. The highly focused beam also allows for localized excitation in a diffraction-limited spot area. The excited SPPs will radiate back into the

glass substrate in the form of leakage radiation at an angle $\theta_{SPP} > \theta_c$, which can be collected through the immersion oil layer via the objective.

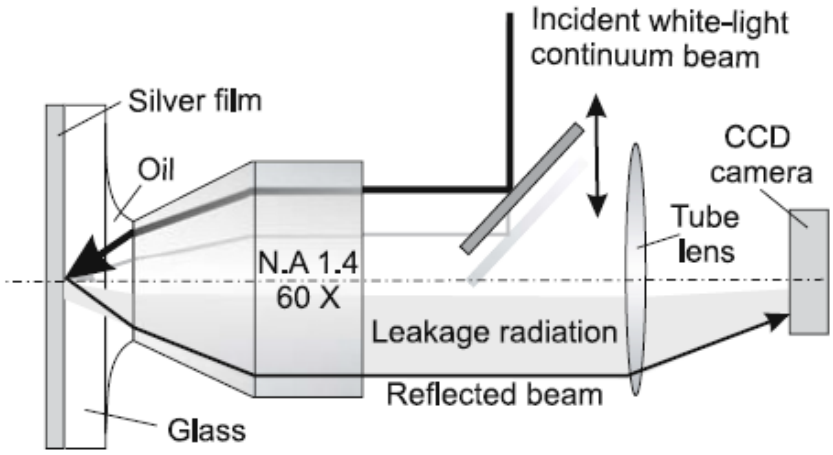

Figure 2.7: Schematic of the excitation of a white-light continuum of SPPs and their observation via detection of the leakage radiation using an index-matched oil immersion lens. Copyright 2005 by the Optical Society of America.

This scheme is especially convenient for the excitation of a continuum of SPPs at different frequencies and the subsequent determination of their propagation lengths.

2.5 Summary

In this chapter, the fundamentals of plasmonic resonance are presented. Surface plasmon polaritons and its loss mechanism is essential for designing and understanding the operation of room temperature plasmonic laser. In this chapter, we have also briefly discussed the origin and excitation mechanism of SPPs.

CHAPTER 3

Plasmonic Laser

Laser is today a basic and common optical device for its usage as a coherent, intense and highly focused light source. But sizes of most of the semiconductor and other photonics based laser are limited by the diffraction limit of light. Plasmonic laser has been introduced in this respect for developing nanoscale sized laser. In this chapter we will cover basic operating principle of laser, idea of diffraction limit and different aspects and challenges of plasmonic lasers and way of addressing those challenges.

3.1 Basic principle of Laser Operation

The quantum theory of electromagnetic radiation predicts the absorption and emission of radiation whenever an atom transitions between two possible quantum states. For simplicity let us consider a 2-level atom with a lower state 1 and upper state 2 (Figure 3.1). Generally speaking, when radiation gets absorbed, the atom switches from the lower to the upper state and emits the stored energy in the reverse process. The atom cannot spontaneously jump from the lower to the upper level. Thus, absorption requires incoming radiation in order to make the upward transitions (left of Figure 3.1). We therefore are allowed to call “absorption” more precisely “stimulated absorption”. Let A be the Einstein coefficient for spontaneous emission. The transition probability therefore

is proportional to the number of electrons in the upper level, namely N_2. Thus the change of electrons in the upper level due to spontaneous relaxation processes can be written as,

$$\frac{dN_2}{dt} = -A_{21}N_2 \tag{3.1}$$

where the indices "21" denote the transition from level 2 to level 1. Solving equation (1) yields the solution for $N_2(t)=N_2(0)\ exp(-A_{21}t)$ with $\tau=1/A_{21}$, where τ is the natural radiative lifetime of the excited state.

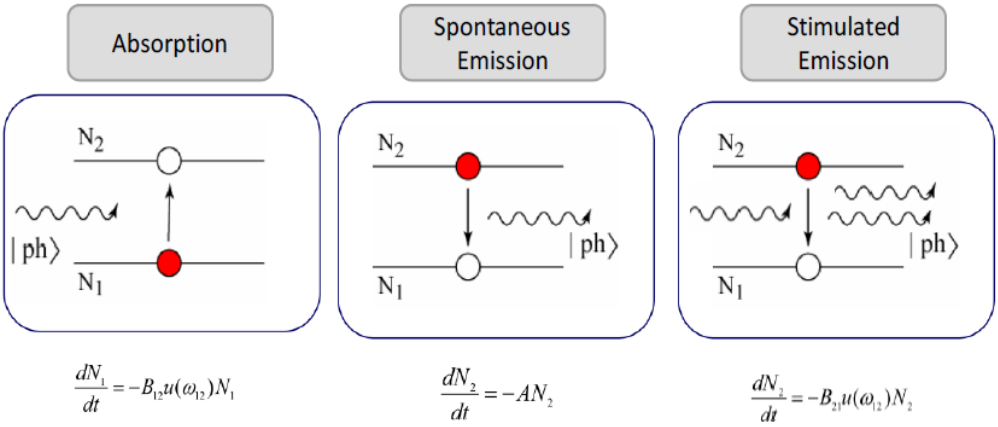

Figure 3.1: Fundamental Ways of Light-Matter-Interaction.

Absorption can be characterized by Einstein's *B* coefficient. Thus we model the absorption rate for electrons in the lower level via Eqn. (3.2) as,

$$\frac{dN_1}{dt} = -B_{12}N_1u(\nu) \tag{3.2}$$

where $N_1(t)$ are the number of electrons in the lower level at time *t*, B_{12} the Einstein coefficient for the transition and $u(\nu)$ the energy density (in units Jm^{-3}) of the incoming electromagnetic wave with frequency ν.

The last process for light-matter interactions is stimulated emissions (right of Fig. 3.1), where excited electron in the upper state can be triggered to transition to the lower state by an incoming electromagnetic wave. Since stimulated emission is a coherent effect the resulting emission is spectrally and temporally coherent to the incoming radiation. Thus, if an atom is paced inside a cavity, which builds up preferential wavelengths (cavity modes with a mode spacing equal to the free-spectral-range of the cavity), lasing operations can be reached. Stimulated emission is governed by the Equation (3.3),

$$\frac{dN_2}{dt} = -B_{21}N_2u(\nu) \tag{3.3}$$

The rate of upward transitions has to equal the rate of all downward transitions yielding equilibrium for a steady-state situation. This steady-state situation can be expressed as shown in equation 3.4,

$$B_{12}N_1u(\nu) = A_{21}N_2 + B_{21}N_2u(\nu) \tag{3.4}$$

This thermal equilibrium can be used to describe the energy levels of the atom in the steady state case. The ratio of N_2 to N_1 will therefore be governed by the thermal Boltzmann law,

$$\frac{N_2}{N_1} = \frac{g_2}{g_1}\exp\left(-\frac{h\nu}{k_BT}\right) \tag{3.5}$$

Here, g_1 and g_2 are the degeneracies of the two levels respectively and k_B the Boltzmann constant. With the electromagnetic radiation following the Planck formula,

$$u(\nu) = \frac{8\pi h\nu^3}{(c/n)^3}\frac{1}{\exp\left(\frac{h\nu}{k_BT}\right) - 1} \tag{3.6}$$

Now, for laser opeartion to take place there must be a active medium which emits radiation in the required region of electromagnetic spectrum. And for true laser oscilallation there must be a optical feedback at the at ends of the gain medium to form a resonant cavity. Now the gain of the resonant cavity can be calculated as,

$$k(\nu) = (N_2 - \frac{g_2}{g_1} N_1) \frac{B_{21} h\nu n g(\nu)}{c} \quad \textbf{(3.7)}$$

Here, g(ν) is the lineshape function of the gain medium. Now, assuming g_2=g_1 from equation 3.7 it can be seen that, for the gain of the resonator to be positive N_2 should be larger than N_1. This condition is known as population inversion. This condition is obtained by the pumping the system above a certain threshold.

3.2 Diifraction Limit

The formulas of Abbe diffraction limit can be easily reproduced using Fourier Optics [91], while a more intuitive and easier way to obtain them is employing the Heisenberg's uncertainty principle [51-53]. In optics, the principle can be expressed as

$$\nabla k \cdot \nabla x \geq 1/2 \quad \textbf{(3.8)}$$

Which indicates that, to reduce the uncertainty of spatial position, usually the increase of the uncertainty for spatial frequency is required. In homogenous and isotropic media with refractive index n, the uncertainty in the domain of spatial frequency is restricted by $\Delta k \leq 2\pi n/\lambda_0$ where λ_0 is the wavelength in vacuum. Then according to equation (3.8), the uncertainty in the domain of spatial frequency satisfies:

$$\nabla x \geq \frac{\lambda_0}{4\pi n} = \frac{\lambda_{eff}}{4\pi} \quad \textbf{(3.9)}$$

Which is very similar to what was derived by Abbe and Rayleigh [54,55].

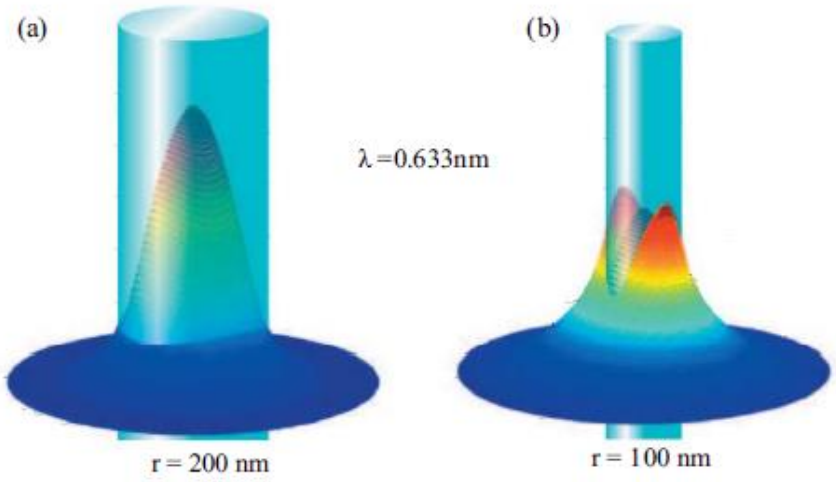

Figure 3.2: The Poynting vector distribution for the fundamental mode of silica nanowires of radii of (a) r = 200 nm and (b) r = 100 nm. The free space wavelength is λ = 633 nm. After Ref. [liu,8].

The usual way to visualize the diffraction limit is to show the focal spot of a lens, as was done in Refs. [51,52]. Here we visualize it in an alternative way through the basic properties of conventional waveguides. In Fig. 3.2 we show the energy confinement of the fundamental modes of silica nanowires of two deferent radii. When the wire diameter is comparable to the effective wavelength of the light in silica (≈ 420 nm), most of the energies can be still confined within the nanowire [Fig. 3.2(a)]. However, when we reduce the diameter of the silica wire to be significantly smaller than the effective wavelength, most of the energy will spread out of the nanowire, as this simple waveguide will not be able to confine the light beyond the diffraction limit [Figure 3.2(b)]. In this respect plasmonic waveguides are very much useful in confining the light to the sub

diffraction scale. While traditional waveguides can confine mode at best in a area of $\lambda^2/4$, plasmonic waveguides can confine mode in a area of $\lambda^2/400$.

3.3 Purcell effect

The Purcell effect is the enhancement of a fluorescent molecule's spontaneous emission rate by its environment [56]. From the three possibilities of how an electromagnetic wave can interact with matter spontaneous emission was thought for a long time as "un-engineer-able" since, as the name suggests, the emission occurs statistically and unpredictably. While this is still true, Edward Purcell proposed in 1946 that spontaneous emission, however, can be modified namely the spontaneous emission rate, γ , can be accelerated or decelerated [57,58]. His analysis predicted that if an intrinsic radiative spontaneous emission process has a rate of, γ_0, that an rate enhancement can be achieved that is given by the Purcell factor $F_p = \gamma_{enhanced}/\gamma_0$. The factor or rate enhancement can be analytically calculated by dividing the solution of the dipole's emission rate into e.g. a cavity by its free space emission rate as,

$$F_p = \frac{\gamma_{cav}}{\gamma_0} = \frac{3}{8\pi}\frac{\lambda^3}{V_{eff}}Q \qquad \textbf{(3.10)}$$

Here, λ is the free space wavelength of the corresponding electromagnetic wave, Q and V_{eff} are the quality factor and mode volume of the cavity respectively. The resulting term for F_p indicated two findings: (i) if the cavity Q-factor is large and/or (ii) the cavity or mode volume is small then the effect is emission rate is enhanced The former realization led many micro cavity research teams to strive to optimize the cavity quality Q-factor [59]. However similar or even stronger enhancements can be achieved if

the Q-factor is moderate or even small, but the cavities' volume is being shrunk into the deep sub-wavelength scale. This is the regime where plasmonics unfolds its potential; the lossy character of plasmonics is rather unimportant compared to its potential to strongly enhance optical fields and compress them into nanoscale volumes [60, 61, 62, 63].

3.4 Plasmonic Nano-Cavities

An optical cavity is essentially a resonator for electromagnetic fields and it is an essential part of the construction of a laser. If at least one dimension of the cavity is longer than the diffraction limit of light, a standing wave can form inside the resonator. Thus, a cavity stores electromagnetic energy in space and time. The cavities quality Q factor relates to the cavities feedback mechanism; the higher the cavity's mirror reflectivity, the higher is the Q-factor, and thus the sharper the resonance (spectrally). We can relate this to first principles like the Heisenberg-uncertainty principle, where we know that the product of energy and time must yield a constant. Therefore if a photon is stored inside a cavity for a long time due to high reflecting mirrors (high Q-factor), the electromagnetic field energy built up yields a short or narrow energy response, namely a sharp resonance spectrum. While one goal of cavity research is to shrink the cavity from macro sizes into the micro regime, a second goal is to increase the cavity's feedback at the same time.

However in terms if scaling photonic cavities, the diffraction limit of light ($\lambda/2n_m$), where n_m is the effective mode index, places a natural lower volume limit. Thus, if the goal is to enhance the light matter interaction it was perceived to optimize the Q-factor rather than scale the cavity beyond the diffraction limit. Empirically we also find

that generally the higher the quality-factor, the larger the cavity volume is, and vice versa [64].This is a trade-off parameter for photonic devices which has to be optimized. With the aim to enhance the light-matter interaction with the use of a cavity, the high-Q approach was taken by many research groups. But in certain plasmonic structures the Purcell factor is improved by shrinking down the mode volume down to sub-wavelength scale while maintaining moderately low Q factor.

3.4.1 Improving Q/V Using Plasmonic Cavities

To overcome the intrinsic metallic loss in plasmonic devices a high q/v ratio is needed. Empirical one finds a proportional relation between a cavity's quality factor and its volume (upper right Figure 3.3); increasing one requires increasing the other [64]. Aiming for strong light matter-interactions and high Purcell effects a possible approach is to decrease the volume for low to medium quality factor ('sweet spot' Figure 3.3). While Photonic cavities (blue circle Figure 3.3) can provide high cavity qualities due to their low loss trapping the photon for long times inside the cavity such cavities are bound to the diffraction limit of light, $(\lambda/2)3$ [65] . Within this context, a second approach is pursued towards achieving high Purcell factors [66]. Using plasmonics, the cavity volume can now be shrunk beyond such diffraction limit sizes (red circle Figure 3.3). The cost for such small nanoscale cavities is the ohmic loss associated with surface plasmon polaritons, which limits the cavity's quality factor. Thus the ideal placement in this 2-parameter space is high-Q, but low volume, therefore on the lower right corner of Figure 3.3 on the upper-right panel, noted as 'sweet spot'. Various cavities towards this goal were explored. Miyazaki et al. for instance deployed an "organ-pile" style plasmonic

cavity with an ultra-small mode volume [67]. However, the cavities resonance is barely discernable from the spectra, leading to a Q-factor of about 10. A second approach was to deploy a distributed Bragg mirror in conjunction with a plasmonic cavity [68]. While this approach yielded an increased quality, the far extending Bragg-mirrors resulted in a large cavity volume.

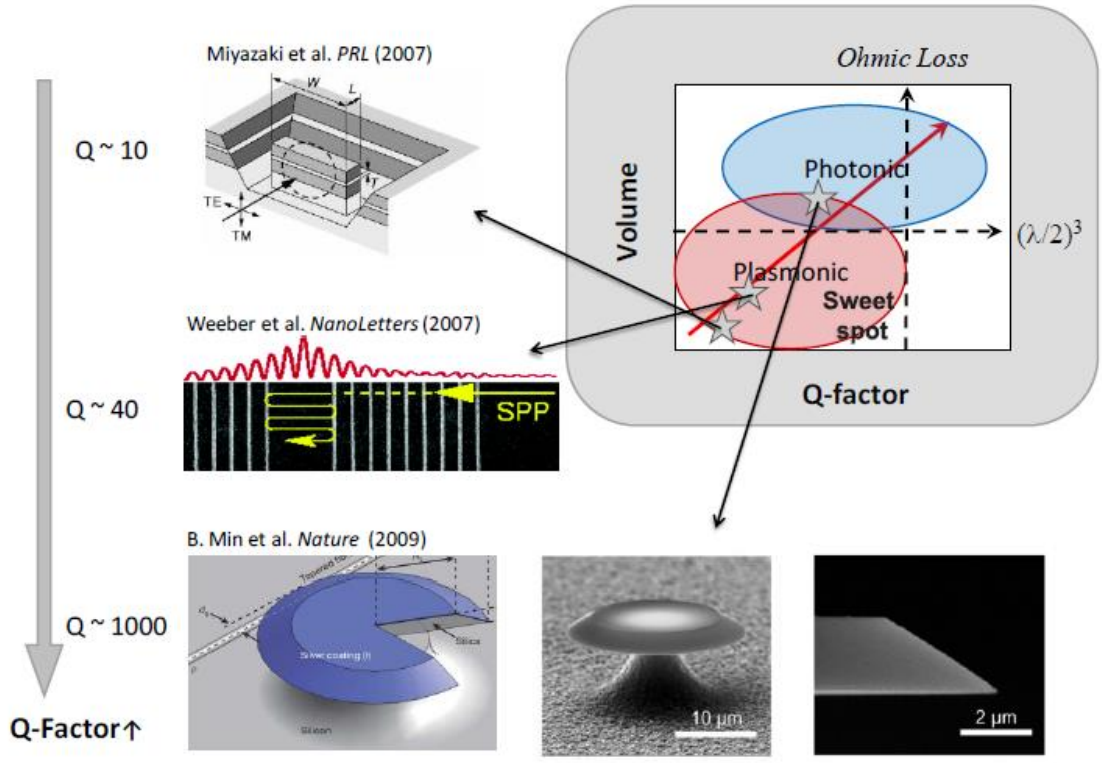

Figure 3.3: Nano-and Microscale Plasmonic Cavities.

In a third approach an axisymmetric whispering-gallery high-Q SPP microcavity that can be implemented by coating the surface of high-Q silica micro-resonators with a thin layer of noble metal was demonstrated [69]. The SPP eigenmodes, as well as the dielectric eigenmodes, are confined within the whispering gallery microcavity and

accessed evanescently by using a single strand of low-loss tapered optical waveguide. This coupling scheme provides a convenient way for selectively exciting confined SPP eigenmodes, with up to half of the input power transfer, which is made possible by phase-matching control between the microcavity SPP and the tapered fiber eigenmodes [69]. However, a fundamental bottleneck for the realization of SPP nano-optical functional devices stems from large intrinsic metal loss at optical frequencies induced by resistive heating. Hence, any type of plasmonic resonator based on a plasmonic waveguiding principle is inevitably limited by the intrinsic metal loss in addition to other sources of losses, such as roughness induced scattering, radiation into free space and the substrate, and bending-induced radiation. While other types of plasmonic cavities can be built, whispering-gallery resonances, which are observed in circular or elliptical resonant structures, are especially attractive due to their extremely large photon lifetime. The smaller optical mode volume can be engineered with the proposed structure when compared to the bare silica toroidal microcavity with a sacrifice in the Q-factor [69].

While these three plasmonic cavity demonstrations show the trend of increasing cavity qualities, Q, their mode volume, V, is also increasing along with the quality factor. Thus the ratio of Q/V is not significantly enhanced, if at all. In the following section we will be discussing a plasmonic cavity demonstration that exhibits a cavity volume below the diffraction limit of light, but still maintains a medium quality factor [70]. This is possible due to both the realization of strong surface plasmon reflectors and low-loss nano fabrication.

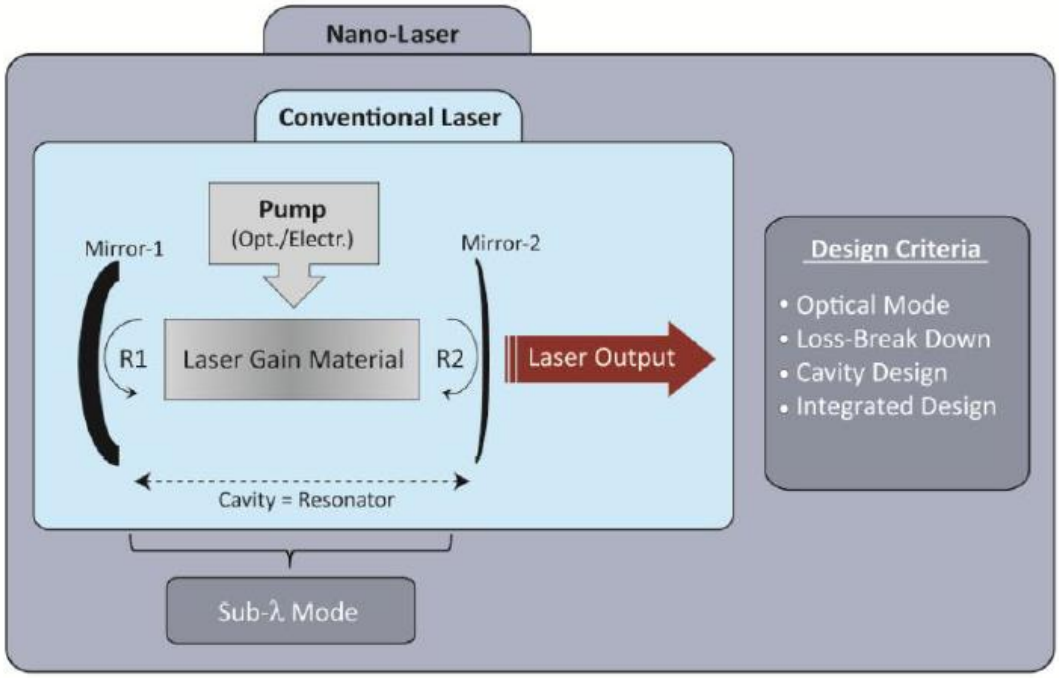

Figure 3.4: Laser Ingredients: Conventional vs. Nano-scale Design.

3.5 Plasmonic Nanolaser

Let us briefly establish the framework for general laser components and what design tasks this implies for Nanolaser devices (Figure 3.4). Starting from the internal mechanism of stimulated emission, the minimum of a 2-level electronic system (e.g. the semiconductor band-gap) is required, provided by the gain material. The required population inversion of electrical carriers can be achieved by either optically or electrically exciting electrons from the lower to the upper level. With increasing photon density inside the laser cavity, stimulated emission events become dominant over spontaneous emission. With a good optical mirror reflectivity the laser cavity provides sufficient feedback, whereas the high density of states of the gain material allows for a

high photon density probability, such that the sum of the optical losses can be overcome and lasing operation is possible.

Challenges in designing are not only limited to the cavity size alone which has to support a sub-wavelength scale optical mode, but also the feedback mechanism has to be addressed as well as considerations of how to pump the device, what materials are suitable from an optical, electrical and integration point of view. The realization of a nanolaser per se requires a very integrated and ‘smart’ design, since the design window yielding to photonic, electronic and material demands is quite small.

One of the first Nanolaser designs was a proposal by Bergman et al., where a laser device was proposed that utilized coherent amplification of localized SPPs [71]. Key point was that the localization of the optical mode can lead to overcome the low feedback system of the lossy metal. The demonstrations of the spaser concept many years after the first spaser proposal indeed showed that it is possible to realize such novel laser concept. With the ultra small optical cavity size, came another advantage of Nanolasers; the ratio of the cavity lifetime (cavity quality) and the cavity volume quantifies the enhancement of the spontaneous emission rate of the pumped gain medium, in other words, a reasonable Q-factor cavity with an ultra small mode volume. Detailed analysis of this effect in plasmonic Nanolaser systems predicts ultra fast direct laser modulation capabilities ranging into the THz regime, far exceeding conventional systems [72]. Thus, key to demonstrating down-scaling laser devices beyond the diffraction limit can be achieved via increasing the optical confinement. The resulting implications are that the fundamental light-matter interaction, i.e. the engine driving the laser, can be engineered

and strengthened towards providing viable paths towards actual Nanolaser device demonstrations. The resulting architectures are able to provide unprecedented laser physics in two domains: time and space.

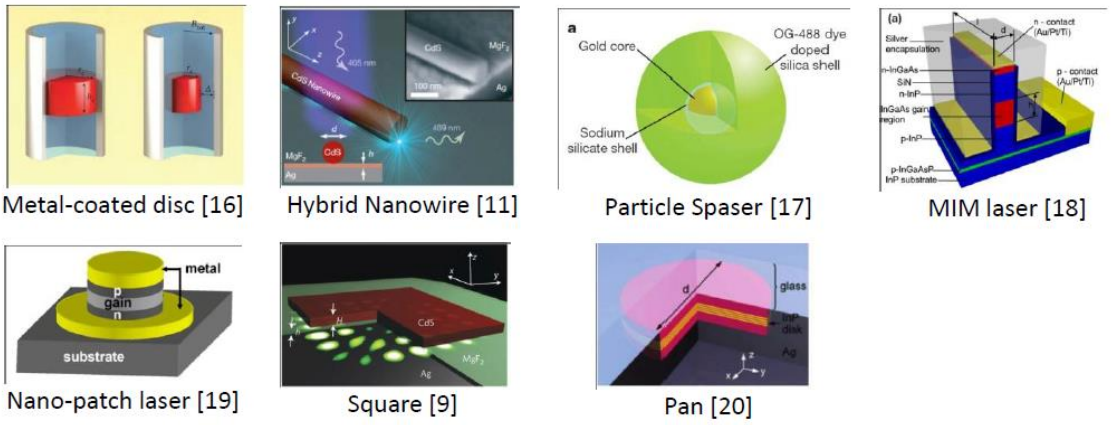

Figure 3.5 : Nanolaser Device Zoo. A general device classification based on the optical lasing mode type leading to Photonic and plasmonic laser architectures. The former one can realize mode sizes approaching the diffraction limit of light without the need for large footprint mirrors like DBRs in Photonic crystal cavity lasers. Plasmon Nanolaser designs come in different flavors featuring one, two or three dimensional optical confinement.

There are already quite a number of papers published on metallic Nanolaser devices including metal-coated photonic laser and plasmon laser (Figure 3.5), which we will review in the following section.

3.5.1 Metal coated photonic lasers

For a conventional photonic laser cavity, the confinement of the cavity mode inside the gain material is due to the index contrast of the gain materials and surroundings. The overlap of cavity mode and gain material will decrease when one or more dimension of the cavity approach the diffraction limit, which will decrease the mode gain volume and increase radiation loss dramatically. A coated metal layer can

shield the cavity modes and thus reduce the radiation loss, though it introduces metal ohmic loss into the system. If the reduced radiation loss is higher than the metal ohmic loss, a coated metal layer can still help to reduce the total loss, which allows for scaling down the photonic cavity close to the diffraction limit of light.

In 2007, Hill et al. reported a metal-coated photonic laser with a diameter semiconductor gain pillar of about 200–300 nm [73]. The pillar is fabricated by etching InP/InGaAsP/InGaAs layers grown via MOCVD epitaxially through electron beam lithography, lift off and an etching process. Then, a silicon nitride layer and metal layers were deposited onto the pillar in sequence. The lasing mode of the metal coated pillar cavity is a HE11-like mode. Since the cavity resonance is below the cutoff frequency for lateral confinement confines the mode effectively in the vertical direction. The overall optical losses of the device were relatively high, since under electrically pumping, the devices only lased at low (10 K and 77 K) temperatures, with an emission wavelength around 1.4 micrometer. Nezhad et al. adjusted this configuration to operate the laser at room temperature by increasing the diameter of the semiconductor gain core and the thickness of the dielectric layer [74]. Yu et al. reported another configuration of metal coated photonic laser, a nanopatch laser [75, 76]. In the nanopatch laser, a semiconductor disc serving as the gain media is sandwiched between a circular metal patch and a ground metal plane.

3.5.2 Plasmon Laser

Another type of a metallic laser is plasmon laser, which generates and amplifies surface plasmons in a plasmonic cavity directly. Surface plasmons, collective electronic

oscillations of metal-dielectric interfaces, are capable of extremely strong confinement well below the diffraction barrier [43]. Such new class of coherent wave source can be considered to be a SPASER (Surface Plasmons Amplification by Stimulated Emission of Radiation) as it was originally introduced by D. J. Bergman 2003 [71]. After being proposed for 8 years, plasmon lasers have been realized in varies kind of plasmon cavities, including metal-insulator-Metal [73], semiconductor-insulator-metal [61,12], semiconductor-metal [76] and localized metal nanoparticle cavities [77]. We will introduce the first three plasmon laser configurations together before talking about the localized metal nanoparticle cavity, since they all share propagating surface plasmon polaritons. In this thesis, we have simulated two room temperature nanolaser: a nanowire structure and a nanosquare structure. We now present the challenges behind the room temperature operation a plasmonic laser and probable techniques to overcome them.

3.5.3 Room Temperature Plasmon laser

Metallic plasmon laser cavities generally exhibit both high metal and radiation losses, limiting the operation of plasmon lasers to cryogenic temperatures, where sufficient gain can be attained. Here, we present room temperature semiconductor sub-diffraction limited laser by adopting total internal reflection of surface plasmons to mitigate the radiation loss, while utilizing hybrid semiconductor-insulator-metal nano-squares for strong confinement with low metal loss. This hybrid structure with dielectric layer between the gain medium and the metal ensure high confinement and helps to overcome the metal loss at room temperature. High cavity quality factors, approaching 100, along with strong $\lambda/20$ mode confinement lead to enhancements of spontaneous

emission rate by up to 18 times. By controlling the structural geometry we reduce the number of cavity modes to achieve single mode lasing. the demonstration of sub-diffraction limited semiconductor plasmon lasers operating at room temperature remains a major hurdle owing to the problem of mitigating both the high absorptive loss of metals and the low cavity feedback of propagating surface plasmons in small metallic structures. This has restricted such lasers to working at cryogenic temperatures in order to attain sufficient gain [73, 12]. Recent efforts in semiconductor plasmon lasers were only able to partially tackle these obstacles and the design stratagems remain mutually exclusive: improved feedback was obtained in devices capped in metal at the expense of high metal loss resulting in limited mode confinement [73]; whereas nanowire lasers on planar metal substrates achieved reduced metal loss but had limited feedback that required cavity lengths much longer than the wavelength [12]. Room temperature plasmon laser operation below the diffraction limit demands effective cavity feedback, low metal loss and high gain; all within a single nano-scale device.

The room temperature plasmon laser and is 45 nm thick, 1 μm length sitting atop a Silver substrate with a 5 nm MgF2 gap. The close proximity of the high permittivity CdS square and silver surface allows modes of the CdS square to hybridize with SPPs of the metal-dielectric interface, leading to strong confinement of light in the gap region (middle Fig. 3.6) with relatively low metal loss [60]. The coupling is extremely strong and causes a dramatic increase in the momentum with respect to the modes of the CdS square alone (middle blue arrow in Figure 3.6). Since the dominant magnetic field component of the waves is always parallel to the metal surface we call these transverse

magnetic (TM) waves [78]. On the other hand, waves with dominant electric field parallel to the metal surface (transverse electric, or TE) cannot hybridize with SPPs.

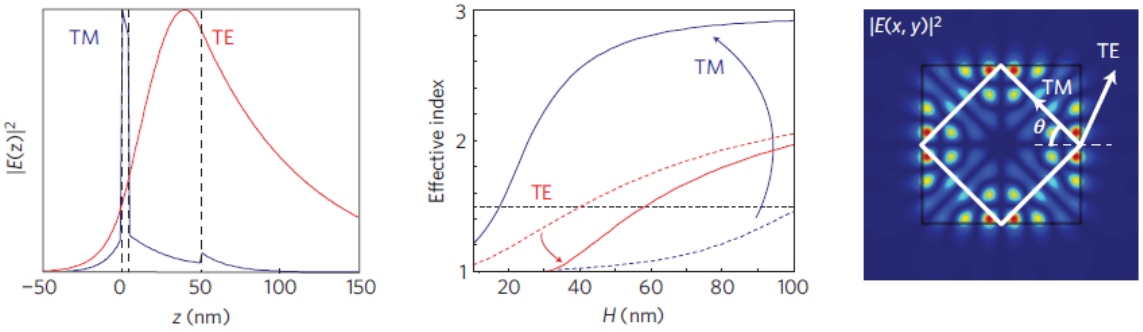

Figure 3.6: Mode Selection of Cavity. (Left) The electric field intensity distribution of the two modes of the system along the z direction. (Middle) The effective index of TM and TE waves with (solid line) and without (dashed line) the metal substrate. (Right) Electric field intensity distribution of a TM mode in the x and y directions. While both mode polarizations are free to propagate in the plane, only TM modes have sufficiently large mode index to undergo efficient total internal reflection providing the feedback for lasing.

Consequently, they become increasingly de-localized as the gap size decreases and are effectively pushed away from the metal surface (left Figure 3.6) with a corresponding decrease in momentum with respect to TE waves of the CdS square alone (middle red arrow in Figure 3.6). While both wave polarizations are free to propagate in the plane, only TM waves have sufficient momentum to undergo total internal reflection and achieve the necessary feedback for lasing as shown in Figure 3.6 [79, 73].

3.6 Summary

In this chapter some of the fundamental principle of laser and photonic devices are discussed. We also presented the problem regarding designing nanoscale laser and some probable solutions to overcome them. In this regard, short discussion on Purcell effect, cavity quality factor are presented. Main obstacles towards implementation of room temperature plasmonic laser and some of the recent approach to address them are also presented.

CHAPTER 4

Simulation Methodology

In this work, we simulated two room temperature plasmonic laser structures. For the simulation purpose, finite difference time domain (FDTD) methodology is followed. Compared to frequency domain method, FDTD method provides a number of advantages. Though several commercial numerical tools are available for time domain and frequency domain analysis which can be used to analyze a plasmonic/photonic structure, every such tool comes with certain limitation in regard to custom geometry or simulation conditions. Moreover, material modeling, definition of different parameters is some of the key aspects of customized simulation. Among a number of commercial softwares, we chose Lumerical FDTD Solutions based on finite difference time domain (FDTD) algorithm. In this chapter, brief introduction to FDTD algorithm is presented. It is followed by discussions on few important simulation parameters and preferences in Lumerical FDTD solver.

4.1 Finite Difference Time Domain Model

Finite-difference time-domain is a numerical analysis technique used for modeling computational electrodynamics which is based on the simultaneous time dependent solution of Maxwell's third and fourth equations which are given by,

$$\frac{\partial \boldsymbol{D}}{\partial t} = \nabla \times \boldsymbol{H} \tag{4.1}$$

$$\frac{\partial H}{\partial t} = -\frac{1}{\mu_0}\nabla \times \boldsymbol{E} \tag{4.2}$$

The relation between the Displacement vector, D and Electric field intensity is given as,

$$\boldsymbol{D}(\omega) = \varepsilon_0 \varepsilon_r(\omega)\boldsymbol{E}(\omega) \tag{4.3}$$

The FDTD method is a member of the general class of grid-based differential numerical modeling methods (finite difference methods). The time-dependent Maxwell's equations (in partial differential form) are discretized using central-difference approximations to the space and time partial derivatives. These finite-difference equations are then solved in a leapfrog manner. In other words, the electric field vector components in a volume of space are solved at a given instant in time and then the magnetic field vector components in the same spatial volume are solved at the next instant in time. This process is repeated over and over again. This leapfrogging time steps are run a finite number of times depending on the type of source used in the simulation domain. In a seminal paper published in 1966, this method of solving Maxwell's equation was first proposed by Yee [80]. That paper proposed a solution set of finite difference equations for time and space dependent equations for loss-less materials. The commercial electromagnetic simulator used in our work is also based on Yee's algorithm. This algorithm proposed a spatially staggered vector components of the E-field and H-field about rectangular unit cells of a Cartesian computational grid. It was arranged in a way so that each E-field vector component is located midway between a pair of H-field vector components. This grid was later

referred to as Yee grid. Figure 3.1 shows arrangement of Yee grid for three dimensional simulation region. Apart from proposing spatially staggered field vectors, Yee also proposed a leapfrog scheme for stepping in time such that electric field and magnetic field are temporally staggered. As a result, electric field updates are computed halfway of each time-step between consecutive H-field updates and vice versa.

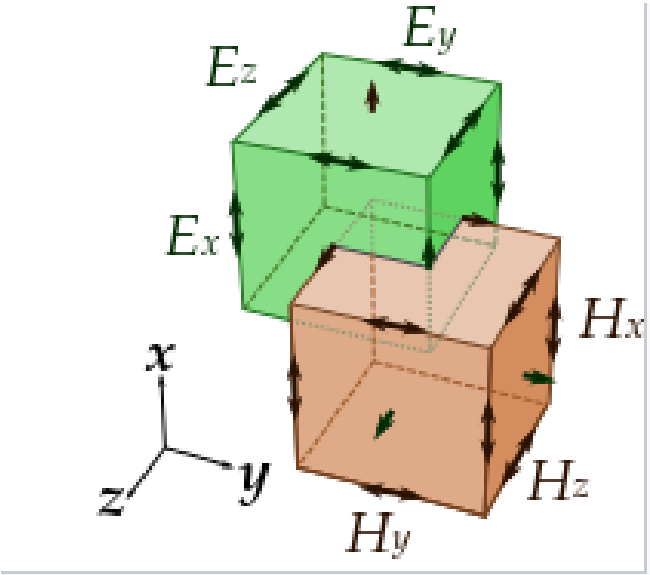

Figure 4.1: Three dimensional Yee grid.

4.2 Source

There are different source model available in the Lumerical FDTD solution. Two of them : Plane wave source and Gaussian source are used for our simulation purpose. These topologies are explained below.

4.2.1 Plane wave source

Plane wave sources are used to inject laterally-uniform electromagnetic energy from one side of the source region. In two-dimensional simulations, the plane wave

source injects along a line, while in three-dimensional simulations the plane wave source injects along a plane. It is also possible to inject a plane wave at an angle. The plane wave source is actually the same object as the Gaussian source, with the only difference being the SOURCE SHAPE setting.

4.2.2 Gaussian Source

A Gaussian source defines a beam of electromagnetic radiation propagating in a specific direction, with the amplitude defined by a Gaussian cross-section of a given width. By default, the Gaussian sources use a scalar beam approximation for the electric field which is valid as long as the waist beam diameter is much larger than the diffraction limit. The scalar approximation assumes that the fields in the direction of propagation are zero. For a highly focused beam, there is also a thin lens source that will inject a fully vectorial beam. The cross section of this beam will be a Gaussian if the lens is not filled, and will be a sinc function if the lens is filled. In each case, the beams are injected along a line perpendicular to the propagation direction, and are clipped at the edges of the source.

4.3 Boundary Conditions

In Lumerical FDTD simulation proper boundary condition setting of simulation region is important for obtaining correct result. Two of the settings metal boundary condition and perfectly matched layer (PML) are presented below.

4.3.1 Metal Boundary Conditions

Metal boundary conditions are used to specify boundaries that behave as a Perfect Electric Conductor (PEC). The component of the electric field parallel to a metal (PEC) boundary is zero; the component of the magnetic field H perpendicular to a metal (PEC) boundary is also zero. Metal boundaries are perfectly reflecting, allowing no energy to escape the simulation volume along that boundary. In the FDE solver, metal BC is the default setting. In plasmonic simulation all the confining surface are defined as metal boundary condition.

4.3.2 Perfectly Matched layer

In plasmonic structures perfectly matched layer (PML) conditions are used in the dielectric surfaces where source light beam is injected. Various types of absorbing boundary conditions may be employed in order to resolve this problem [81 , 82]. The perfectly matched layer developed by Berenger is one of the most effective among all ABCs[83]. The basic idea of the PML technique is to add an additional lossy layer around the simulation region with intrinsic impedance matched with the media at the outermost simulation region which ensures zero reflection from the interfaces and the field is attenuated while propagating through the media. It is ensured that the field intensity attenuates to zero before it hits the simulation boundary. In a continuous space, the PML absorber and the host medium are perfectly matched. However, FDTD simulation, the electric and magnetic material parameters are discretized and are spatially staggered. This results in discretization errors that can affect ideal behavior of the PML. In Lumerical FDTD Solutions, there are a number of topologies for PML to

choose from. In our simulation where obliquly incident light was used, we have implemented stretched coordinate PML formulation [84].

4.3.3 Determining Spatial and temporal Cell Size

An important aspect of electromagnetic simulation with FDTD method is choosing correct values of spatial cell size. Numerical dispersion can occur from discrete spatial sampling of FDTD mesh. Not only that, if meshing is coarse, it can result in slight anisotropy of speed of light on direction of propagation. Determining the cell size is much like sampling a signal. Higher sampling rate results in more accurate representation of the real quantity like any sampling process. At least ten points per wavelength restricts simulation errors to acceptable limit though the minimum number of points per wavelength depends on various factors involving the simulation medium. To ensure this, ten points per wavelength in the material with the largest refractive index in the simulation medium is required to be used. Therefore,

$$\Delta z \leq \frac{\lambda_0}{n_m \times 10} \tag{4.4}$$

Here, ∇z is the spatial cell size, λ_0 is the free space wavelength and n_m is the largest refractive index contained in the simulation medium. Once the cell size has been chosen, the time step is also chosen according to stability considerations. For stability reasons, a field component cannot propagate more than one cell size in the time step Δt. This means that,

$$\nabla t \leq \frac{\Delta z}{\sqrt{n} \times c_0} \tag{4.5}$$

FDTD algorithm allows the use of graded meshes as the value of spatial mesh size is defined by the material index. While requiring less memory and less computation time than uniform mesh such a non-uniform mesh can make FDTD calculations more accurate. Non-uniform meshing allows relatively larger mesh sizes in medium with lower refractive index, while using small meshes in high refractive index material. Apart from non-uniform meshing, Lumerical FDTD provides a number of conformal meshing methods. Conformal meshing a number of mesh refinement options which can give sub-cell accuracy from a simulation. That means, we can get accurate representation of device response using much higher mesh size. In our simulations, we have used non-uniform grids with conformal meshing applied to all materials.

4.4 Dispersive Material Modeling

The ability to produce broadband response of a device in a single simulation is one of the main advantages of finite difference time domain method. However, the dispersion has to incorporate into the material system in FDTD algorithm as different materials exhibits variation of material index with wavelength. FDTD simulators typically employ Drude, Debye, or Lorentz materials. But, these models are highly simplified representation of real materials. As a result, relying on these models for a wide band simulation would result in significant deviation from the actual response. One of the ways to solve this problem is to use multi-pole model, which is a dispersion model that results from combining two or more distinct Lorentz models. This model has some limitations when it comes to modeling real materials impacted by impurities, defects, and

other more complicated material issues. In some electromagnetic simulators, materials are modeled with a polynomial fitting. While this method can provide accurate representation of the model, it is prone to cumbersome calculation and high computational cost depending on the order of the polynomial. To solve this broadband simulation challenge, Lumerical uses multi-coefficient materials (MCMs). MCMs rely on a more extensive set of basis functions to better fit dispersion profiles that are not easily described by Drude, Debye, and Lorentz materials. It also provides designers with the ability to automatically and optimally choose the type and number of terms required to accurately describe their materials. The type of fit that can be automatically generated to imported material data as well, which enables us to model any material as long as the material indices are available. In our simulations of passive and active devices in this work, we have used this multi-coefficient materials to model Ag (Johnson and Christy [45]). The dielectric materials used in our simulation was assumed non-dispersive over the frequency of interest.

4.5 Gain Medium Modeling

In this thesis of simulating room temperature palsmon laser, the laser gain medium was modeled using four level two electron system. This model utilizes simplified quantized electron energies which provide four energy levels for each of the two electrons. This model also takes into account the effect of Pauli's exclusion principle. The population levels of the gain mediums are governed by the coupled rate equations. To simulate the response of gain medium, these rate equations and Maxwell's equations

are self-consistently solved through the FDTD algorithm. In this section we will discuss this modeling methodology.

4.5.1 Four Level Two electron Model

This model of the lasing dynamics is of a four-level two electron atomic system. Our model incorporates simplified quantized electron energies that provide four energy levels for each of two interacting electrons. Transitions between the energy levels are governed by coupled rate equations and the Pauli Exclusion Principle (PEP) [60]. Our new approach is an advance relative to the methods described in [9, 71] which do not include the pumping dynamics for a four-level system, or the PEP. With this semi classical approach, we treat the atom quantum mechanically, and the electromagnetic wave classically [85].

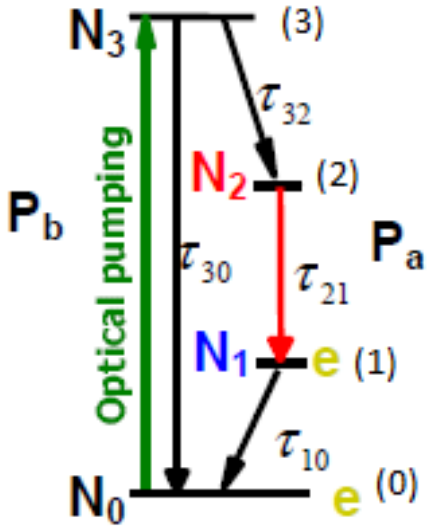

Figure 4.2: four-level two-electron model [chang].

Figure 4.2 shows the four level system used in this formulation. Pumping electromagnetic pulse induces absorption from ground level (0) to highest level (3) from which a fast non-rediative emission increases the population in the higher lasing level (2). Radiative transition between level (2) and level (1) leads to lasing emission if there is population inversion between this two levels. Finally, another non-radiative transition induces emission from level (1) to level (0).

These transitions in this 4 level system are treated as two coupled dipole oscillators. Level 1 and level 2 corresponds to dipole P_a, whereas, level 3 and level 0 corresponds to dipole P_b. Polarization densities P_a and P_b are found to be driven by the product of electric field E and population difference between two corresponding levels, i.e.,

$$\frac{\partial^2 \boldsymbol{P_a}}{\partial t^2} + \gamma_a \frac{d\boldsymbol{P_a}}{dt} + \omega_a^2 \boldsymbol{P_a} = \xi_a (N_2 - N_1)\boldsymbol{E} \tag{4.6}$$

$$\frac{\partial^2 \boldsymbol{P_b}}{\partial t^2} + \gamma_b \frac{d\boldsymbol{P_b}}{dt} + \omega_b^2 \boldsymbol{P_b} = \xi_b (N_3 - N_0)\boldsymbol{E} \tag{4.7}$$

Here, $\xi_{a,b} = 6\pi\varepsilon_0 c^3/(\omega_{21,30}{}^2 \tau_{21,30})$, $\gamma_{a,b}$= damping coefficients, $\omega_{a,b}$ = resonant frequencies. In this formulation, Pauli's exclusion principle (PEP) is enforced. Due to PEP, presence of electron in one energy level reduces the rate/efficiency of pumping or relaxation from other levels. Therefore, the rate of transition is function of both the source and destination population level. Using this principle, the rate equations for the 4 level system becomes,

$$\frac{dN_3}{dt} = -\frac{N_3(1 - N_2)}{\tau_{32}} - \frac{N_3(1 - N_0)}{\tau_{30}} + \frac{1}{\hbar\omega_b}\boldsymbol{E}\frac{d\boldsymbol{P_b}}{dt} \tag{4.8}$$

$$\frac{dN_2}{dt} = \frac{N_3(1-N_2)}{\tau_{32}} - \frac{N_2(1-N_1)}{\tau_{21}} + \frac{1}{\hbar\omega_a}\boldsymbol{E}\frac{d\boldsymbol{P_a}}{dt} \quad \textbf{(4.9)}$$

$$\frac{dN_1}{dt} = \frac{N_2(1-N_1)}{\tau_{21}} - \frac{N_1(1-N_0)}{\tau_{10}} - \frac{1}{\hbar\omega_a}\boldsymbol{E}\frac{d\boldsymbol{P_a}}{dt} \quad \textbf{(4.10)}$$

$$\frac{dN_0}{dt} = \frac{N_3(1-N_0)}{\tau_{30}} + \frac{N_1(1-N_0)}{\tau_{10}} - \frac{1}{\hbar\omega_b}\boldsymbol{E}\frac{d\boldsymbol{P_b}}{dt} \quad \textbf{(4.11)}$$

In Eq. 3.8-11, N_i is the population density probability in level *i*, and τ_{ij} is decay time constant between levels *i* and *j*. These four rate equations are coupled to Maxwell's law through polarization densities, P_a and P_b by the following equation,

$$\frac{d\boldsymbol{E}}{dt} = \frac{1}{\varepsilon}\nabla \times \boldsymbol{H} - \frac{\mathbf{1}}{\boldsymbol{\varepsilon}}\boldsymbol{N}(\frac{\boldsymbol{dP_a}}{\boldsymbol{dt}} + \frac{\boldsymbol{dP_b}}{\boldsymbol{dt}}) \quad \textbf{(4.12)}$$

Therefore, the four rate equations along with this Ampere's law provide a selfconsistent set of equations describing the interactions between gain molecules and electromagnetic fields associated with nano-particles. Using this model, we can simulate different gain mediums if parameters related to emission and absorption characteristics are known. In this work, the gain medium we have used is an organic gain medium, IR-140. The parameters used for this model are as follows:

- ω_a, ω_b : the angular frequencies corresponding to the energy differences of levels 2-1 and 3-0 respectively [Hz]
- t_{30}, t_{32}, t_{21}, t_{10} : the lifetimes of the different decay channels [s]

- N : the electron population density [m^-3]
- SET INITIAL POPULATIONS : 0 and the initial populations are N0=N1=1, and N2=N3=0.

For modeling the CdS gain medium we set the above parameters as, ω_a= 3769.9 THz, ω_b= 4654.2 THz, $\tau_{30}=\tau_{21}$=0.1 ns, and $\tau_{32}=\tau_{10}$= 1 ps, N=1.19 ×10^19 cm−3 [5] and set sampled CdS material as the base material of the four level two electron model.

Similarly, for modeling the ZnO gain medium for the second structure we set the above parameters as, $\omega_{a=}$ 4895.9 THz, ω_b= 5309.73 THz, $\tau_{30}=\tau_{21}$=325 ps, and $\tau_{32}=\tau_{10}$= 1 ps [6] and set sampled ZnO material as the base material of the four level two electron model.

4.6 Summary

In finite difference time domain method, the constituent equations are solved simultaneously to give the time evolution of the different field components in a defined medium. It allows calculating broadband response of a system from a single system by using fourier transform of the system response to a broadband input. Among various commercial simulation tools, we have used Lumerical FDTD Solutions for our work. Lumerical FDTD gives output corresponding to a unit pulse source while our simulation structure needed repeated source. To overcome this limitation we exported the Fourier transform data of the FDTD solution from Lumerical to MATLAB^{TM} software and multiplied by the Fourier transform of the repeated source to obtain the accurate result. We have discussed our choice of boundary conditions and meshing methodologies for

different simulations using this simulation tool. This electromagnetic solver facilitates the modeling of dispersion of passive materials using multi-coefficient models. For laser simulation, a 4 level 2 electron system was used for gain medium. This model was incorporated into the time-stepping algorithm of FDTD.

CHAPTER 5

Simulation Setup & Results

In our work we simulated two experimental works on room temperature Plasmon laser. The first structure is the Ag-MgF_2-CdS nanosquare structure proposed by Ma et al. [5] and the second structure is the Ag-LiF-ZnO proposed by Sidiropoulos et al [6]. Both structures obtain enough gain to overcome the metallic loss at room temperature. Ag

metal is chosen for its comparatively lower loss at room temperature than other novel metal. For simulating the room temperature environment all the population density data for modeling the gain medium and refractive index data were taken of room temperature. In this chapter the detailed simulation setup are presented. Also obtained results are explained with physics and compared to the experimental works.

5.1 Ag-MgF_2-CdS Nanosquare Structure

As shown in Figure 5.1, this structure consists of 45 nm thick, 1 μm length single crystal CdS square atop a silver surface of 300 nm thickness separated by a 5 nm thick MgF_2 gap layer ensuring λ/20 optical confinement. Strong optical feedback was achieved by total internal reflection of surface plasmon at the cavity boundaries resulting in sufficiently higher quality factors than other nanowire lasers [12], which can be identified by pronounced cavity mode even in the spontaneous emission spectrum far below the laser threshold. This feedback mechanism only plasmonic mode since the photonic mode does not have enough momentum for total internal reflection. The square is pumped by frequency doubled, mode locked Ti sapphire laser. (λ_{pump}=405 nm, repetition rate= 10 KHz, pulse length 100fs). A ×20 objective lens (Numerical Aperture=0.4) focuses the pump beam to a ~5 μm diameter spot on the sample. The lasing modes are observed around 500 nm [5].

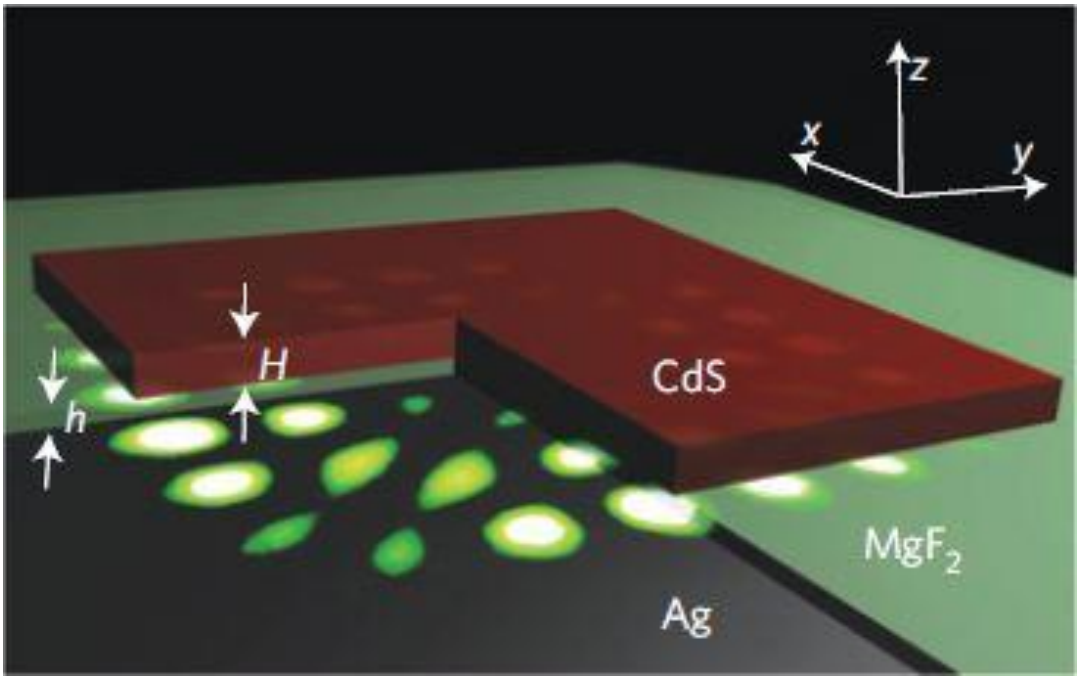

Figure 5.1: Physical structure of the room temperature nanolaser proposed by Ma et al [5].

5.1.1 Simulation Setup of Ag-MgF_2-CdS Room Temperature Plasmon Laser

The silver, MgF2 and CdS layer was created using rectangle structure in a CAD environment in with appropriate dimension as shown in Figure 5.2. 'Johnson and Christy' and sampled data model [86] were used to model Ag and MgF_2 layer respectively to correctly reflect dispersion relations. The light from the plane wave source was passed through a glass ×20 objective lens of NA=0.4 to focus the beam on the sample. SiO_2 is selected as the material of choice for the lens. From numerical aperture and selected entrance pupil, D the focal length, f is calculated to be 11.45 μm. The curvature of radius of the lens and the third radius of the ellipsoid are found to be10.76 μm and 1.2 μm

respectively. The simulation setup is shown in Fig. 3. The cadmium sulfide gain medium was modeled by a 'four level two electron model' [85]. The parameter of the model is set as the wavelength of pumping 405 nm, emission wavelength of 500 nm, μ_{21}= τ_{30} = 0.1 ns(τ_{21}= spontaneous emission lifetime) [87], τ_{32}=τ_{10}=1 ps and population density of CdS at room temperature is used. CdS with sampled data was used as the base material four level two electron gain medium to accurately model the dispersion relation.

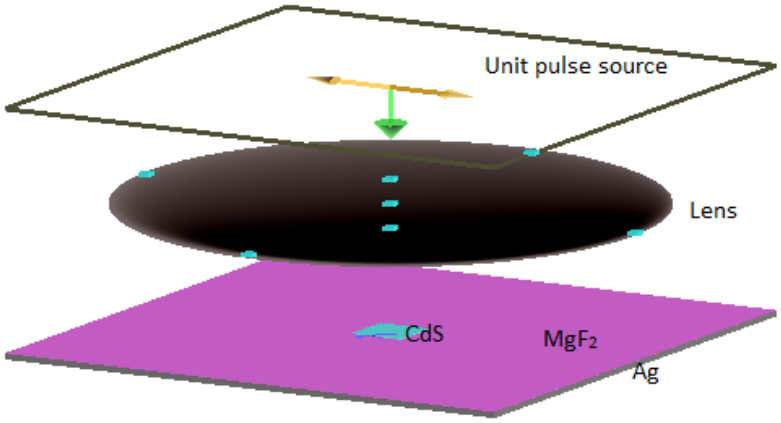

Figure 5.2: Simulation Setup of Ag-MgF_2-CdS Room Temperature Plasmon Laser

The lens is placed 6.25 μm above the CdS to focus the light beam into 5 μm diameter spot on the sample. The simulation region is consists of the metal, insulator and whole portion of the CdS layer. The boundary condition of the simulation region was defined as metal and stretched PML. The maximum mesh cell size is found from the

equation 4.4 is to 16.2 nm and dt value to be .03 fs. But actual maximum mesh cell size is set to much less than the calculated value to ensure better accuracy. ‘auto non-uniform’ is chosen for mesh setting in FDTD settings. The wavelength and pulse width of the light source was set to be 405 nm and 100 fs. At first output intensity spectrum due to a unit impulse source was calculated and multiplied by the Fourier transform of the source signal to obtain the output intensity spectrum due to the total pulse train. Some aspects of the plasmonic laser phenomenon such as modal confinement is evaluated by calculating effective refractive index of a mode. The coupling of the TM mode of the semiconductor slab to the Plasmon of the Metal surface is determined by calculating effective index and electric-field-intensity distribution along the z axis (Figure 5.1). The lasing action is observed by the determining the emission spectrum under different pumping rate. The results obtained from simulation are given below with explanation and comparison with the experimental works.

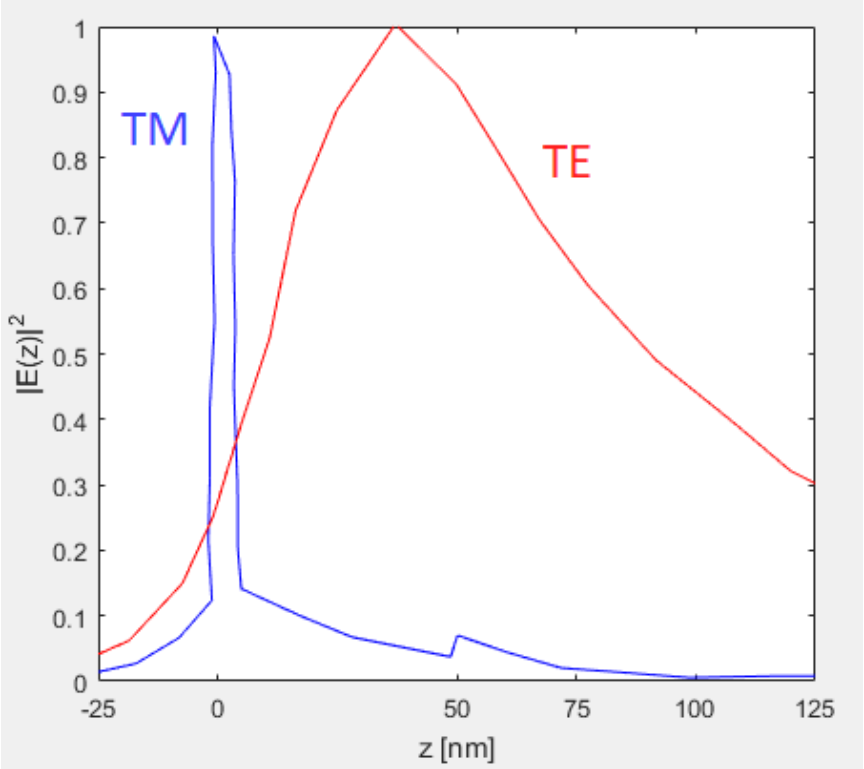

Figure 5.3: Electric field distribution of the two mode along the z direction.

5.1.2 Coupling of The Optical Mode to Surface Plasmon

The plot of the figure 5.3 is obtained by plotting the electric field intensity of the TM and TE mode against the z axis. According to the principle of plasmonics the closeness of the high-permittivity CdS square and silver surface allow the modes of the CdS to couple and share energy with SPPs of the metal dielectric interface. The field intensity of the TM mode increases drastically in the insulator gap layer which can be seen in the Figure 5.3, where the electric-field-intensity is shown throughout the structure along the z axis (Figure 1). This shows the strong confinement of light in the gap region [60]. This coupling of energy helps to overcome the metallic loss at room temperature.

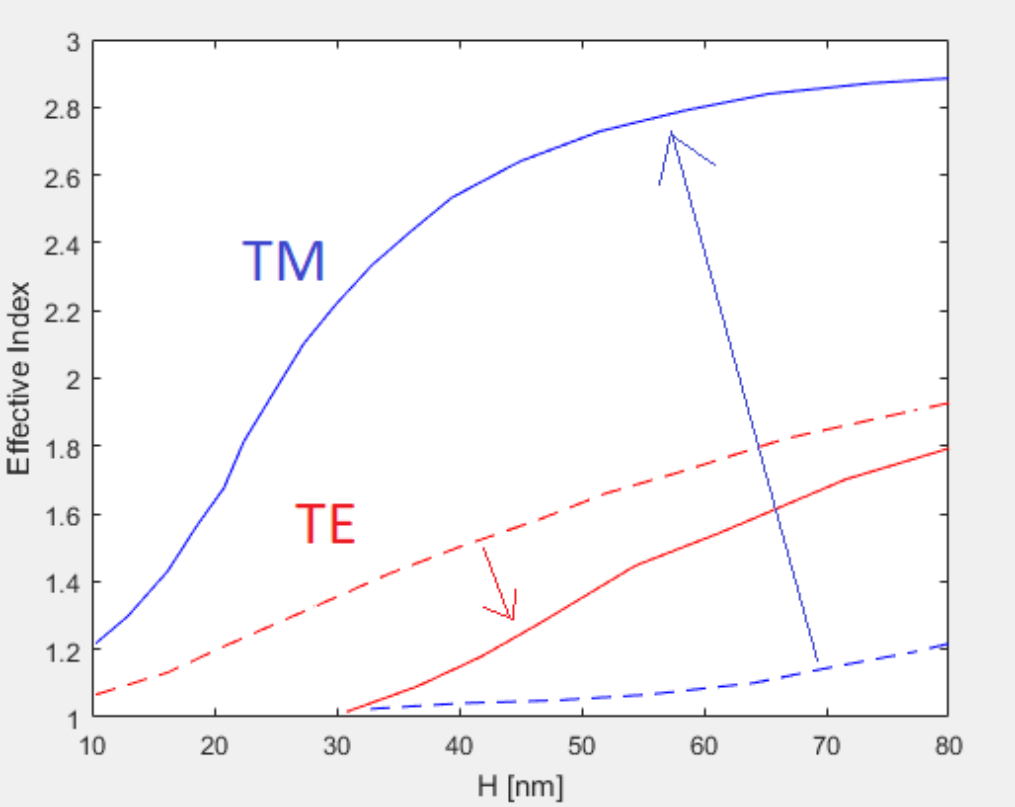

Figure 5.4: Effective index of TM and TE waves of CdS square with (solid line) and without (dashed line) metal substrate.

5.1.3 Total Internal Reflection of TM Mode

The coupling of the optical mode of CdS with surface Plasmon increases the wave-vector and also the momentum, according to the equation, $k_{sp} = k_0\sqrt{\frac{\varepsilon_1\varepsilon_2}{\varepsilon_1+\varepsilon_2}}$. Where, $\varepsilon_1(\omega)$of the permittivity of the silver system, ε_2 is real part of the permittivity of CdS. k_0 and k_{sp} are the wave-vector of the coupled mode of CdS in before and after coupling respectively. In this case the transverse magnetic field waves (dominant magnetic field of which waves are parallel to the metal surface) couples strongly with the surface plasmons and their momentum increases dramatically. Increase of momentum in

turn means increased effective refractive index of the coupled mode. Figure 5.4 shows the increase and decrease of TM and TE modes respectively, after introducing the silver dielectric layer. This plot is made by calculating effective index of the corresponding modes with the increase of the thickness of the CdS layer (H, see Figure 5.1).

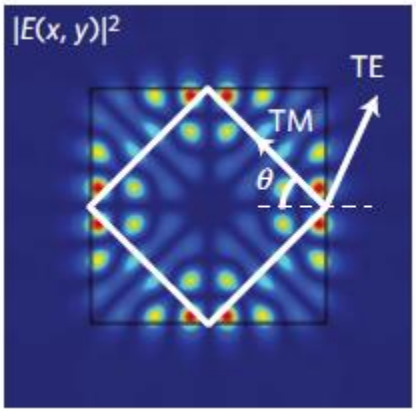

Figure 5.5: Electric field distribution of a TM mode (Image Source:[5])

With the increase of the effective index of the TM mode it has sufficient momentum to undergo total internal reflection and obtain necessary feedback for lasing ([43],[88]). But the TE mode lacks sufficient momentum for total internal reflection and it is also delocalized from surface Plasmon and heavily scattered. The total internal reflection phenomenon is shown in Figure 5.5. Because finite cavity size leads to imperfect internal reflection[89], the laser response is obtained from the volume scattering of radiation waves. The phenomenon of total internal reflection is illustrated in Fig. 5.5(Source: [5]).

5.1.4 Formation of Cavity Modes

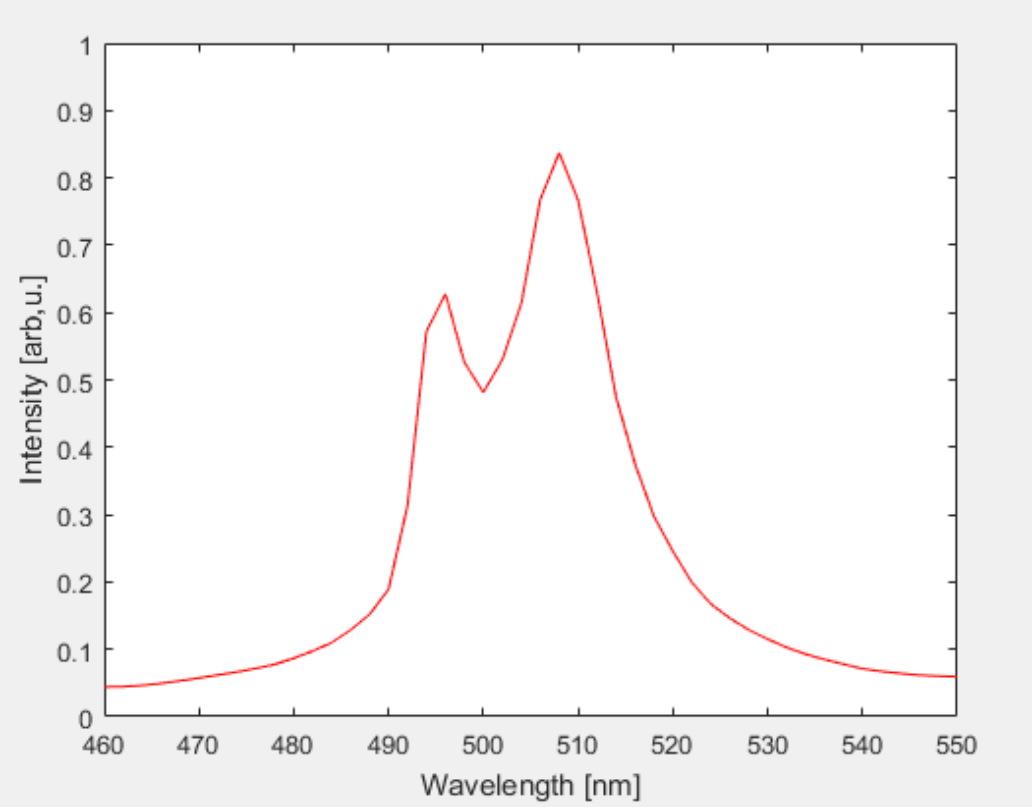

Figure 5.6: Spontaneous emission spectrum of CdS structure at a peak pump intensity of 1900 MW cm-2.

Like any other optical resonator this plasmonic cavity supports a number of modes. The peak of emission spectrum of CdS nanobelt structure is around 500 nm with around 30 nm bandwidth (Fig. 5.7 source: [90]). Those cavity modes whose wavelengths fall under the Photoluminescence curve get amplified. The amplified cavity modes are found by plotting the spontaneous emission spectrum by simulating the system with source of sub-threshold intensity. The emission spectrum at pumping intensity of 1900 MW cm^{-2} found by simulation is shown Fig. 5.6. The Q factor of two pronounced cavity

modes 495 nm and 509 nm are 97 and 38. The latter Q factor is overestimate this resonance is consist of several other modes which are too close to be resolved [5].

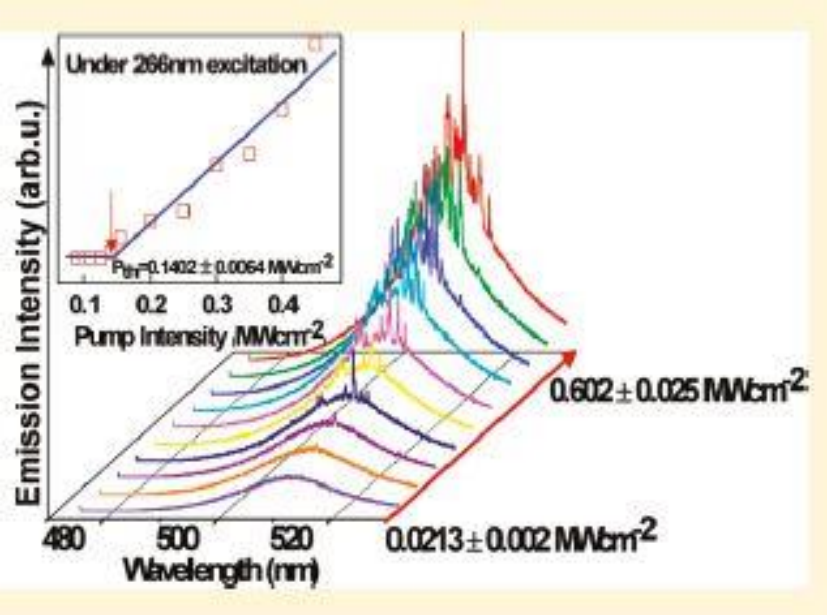

Figure 5.7: Photoluminescence emission spectra of CdS nanobelts [90].

5.1.5 Lasing Action

Spontaneous emission, amplified spontaneous emission and full laser emission occurs at pumping rates of 1900 MW cm^{-2}, 2200 MW cm^{-2} and 3000 MW cm^{-2} respectively. At full laser oscillation a number of higher coherence mode appear. Room-temperature laser spectra are given in Figure 5.8 showing the transition from spontaneous emission(1,900MWcm−2, black) through amplified spontaneous emission (2,200MWcm−2 , red) to full laser oscillation (3,000 MWcm−2, blue). For larger pump intensities, multiple cavity modes appear with orders-of-magnitude-higher coherence than the underlying spontaneous emission, as shown in Figure 5.8. The emission spectrum is completely dominated by these high-coherence peaks when collecting the

light at large collection angles, because the plasmonic cavity modes preferentially scatter into large angles to conserve their in-plane momentum.

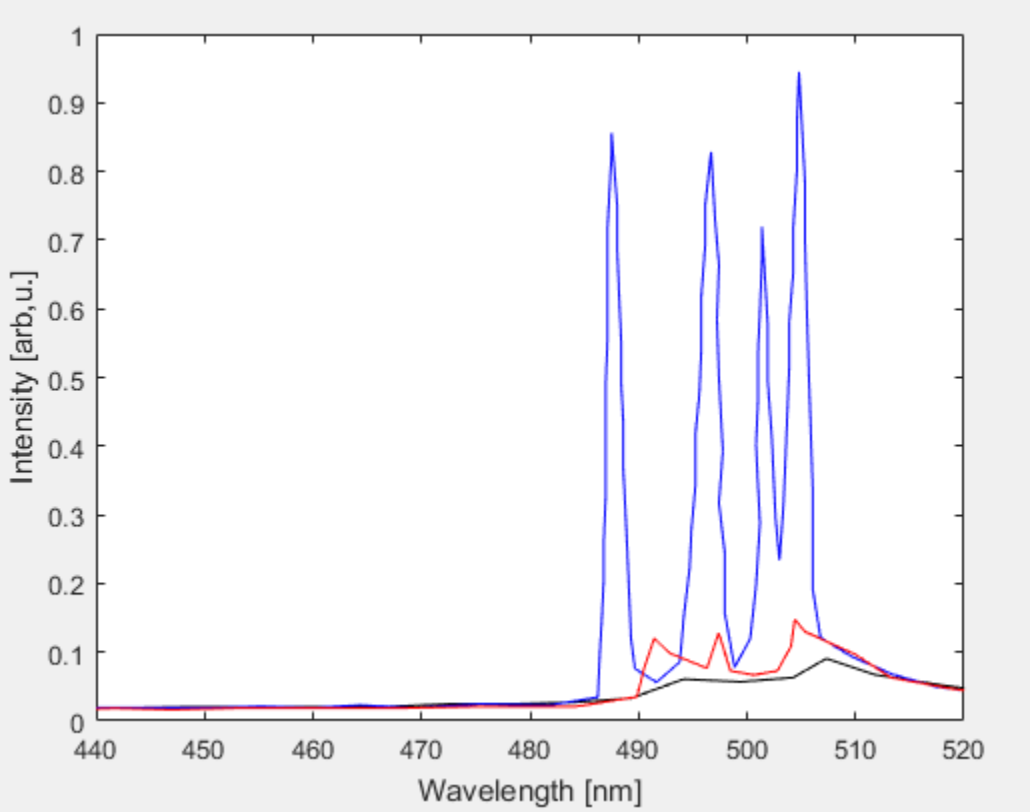

Figure 5.8: Room-temperature laser spectra showing transition from spontaneous emission through amplified spontaneous emission to full laser emission.

5.1.6 Single Mode Operation

If the symmetry of the CdS square is compromised that is if one side of the CdS nanosquare is curved then due to the lack of symmetry only a number of modes can undergo total internal reflection and only one of them corresponds to the Photoluminescence spectrum of CdS nanobelt.

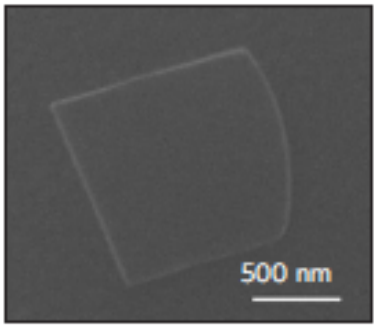

Figure 5.9 Micrograph of the single mode operational structure of the device.

Fig. 5.9 shows the simulation configuration and Fig. 5.10 shows emission spectrum of the laser spontaneous emission, amplified spontaneous emission and full laser oscillation obtained at pump rate of 1,000MWcm−2 (black), 1,200MWcm−2 (red) and 1,400MWcm−2 (blue) respectively. By simulating a CdS of 70 nm thickness and 1.1 μm length lasing action was observed only at 495 nm.

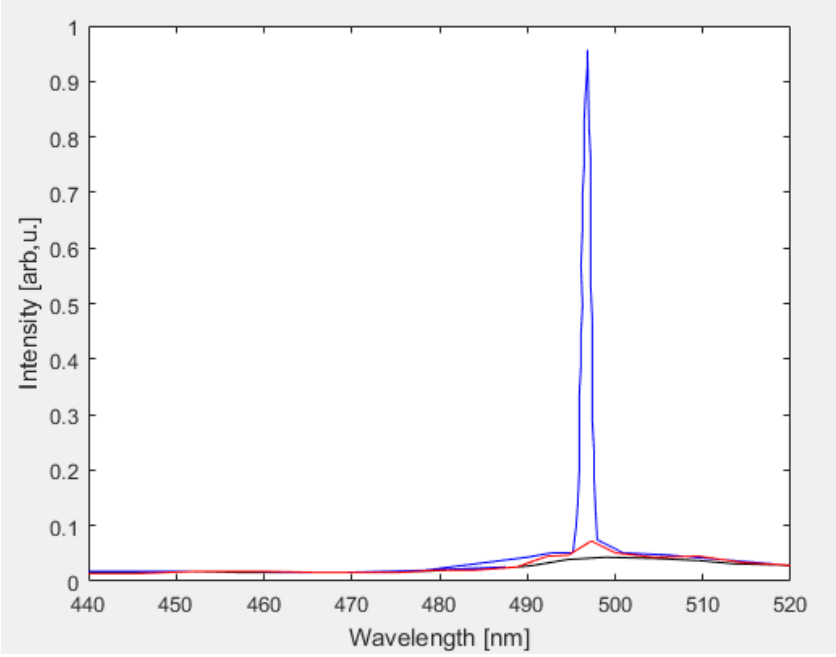

Figure 5.10: Single mode emission at different peak pump intensity.

5.1.7 Purcell Effect

Purcell effect is defined as the enhancement of the spontaneous emission rate of a fluorescent molecule or atom by its environment [56]. Purcell factor in this case was calculated by the equation (1),

$$F = \frac{\gamma}{\gamma_0} \approx F_\infty[1 + \beta L csch(\alpha L/\sqrt{2})] \quad \textbf{(5.1)}$$

Where, $\gamma = \gamma_{sp} + \bar{Q}B$, γ_{sp} is the enhanced spontaneous emission rate compared to γ_0 the usual emission rate of the CdS band edge transition. Other constants of the equation (1) are given as, α=6323 cm^{-1}, β=4.93 $(\mu m)^{-1}$ and F_∞=2.08[5]. In Fig. 5.11 the Purcell factor was plotted against the cavity square circumference, L. Simulation result matches the experimented value up to a high degree of accuracy. As the cavity side length decreases cavity feedback increase as the cavity feedback has no effect beyond the Surface Plasmon Propagation length, δ. High cavity quality factor and strong mode confinement leads to the high Purcell factor as large as 18. This high Purcell factor shows hope in fine investigation of light matter interaction [5].

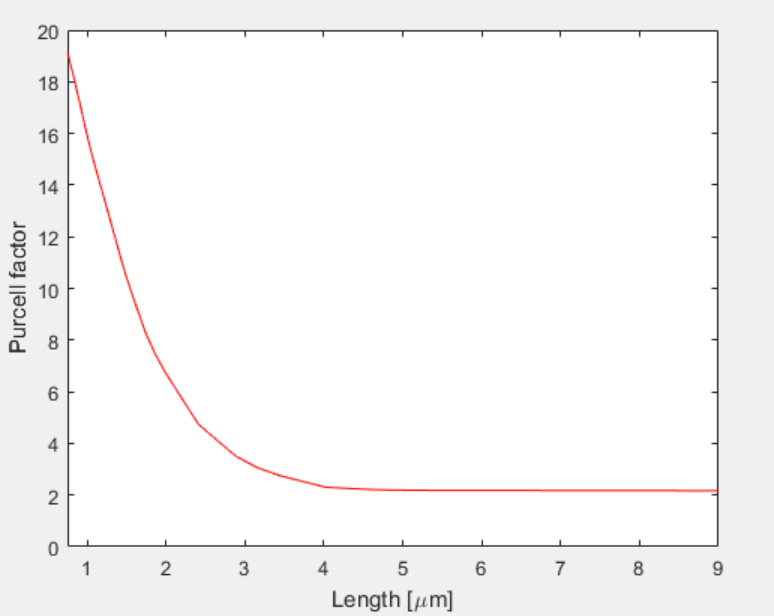

Figure 5.11: Plot of the theoretically calculated Purcell factor.

5.2 Ag-LiF-ZnO Nanowire Structure

The second room temperature plasmon laser we simulated was the Ag-LiF-CdS nanowire structure proposed by Sidiropoulos et al [6]. As depicted in figure 5.12 in this structure a ZnO nanowire of 150 nm diameter is placed atop a 100 nm thick silver layer which itself is placed on a silicon substrate with a 10 nm thick LiF gap dielectric layer. The presence of the dielectric gap layer between the gain medium and the Ag metal causes drastic confinement of light occurs in the gap layer and increases Q factor while decreasing the mode volume. This in turn helps to overcome the metal loss at room temperature. Also Ag metal is chosen for comparatively lower lossy property. The system was pumped by two laser beams with slight delay between them combined through a cylindrical lens (f=300 nm) and ultra violet objective (20× NA=0.4) onto the sample to form a two overlapping elliptical beams. Each nanowire was optically pumped

at 355 nm with 150 fs pulses at a repetition rate of 800 KHz. Because the sp frequencies of silver-air ($\hbar\omega_{sp}$=3.65 eV) and silver-ZnO ($\hbar\omega_{sp}$=2.9 eV) encompasses the exciton energies, excitons couple strongly to the SPPs and thus light of this energy gets two dimensionally confined amplified through A Fabry Perot resonator formed between two end facets of the structure. Lasing action from this structure is observed at room temperature at 385 nm [6].

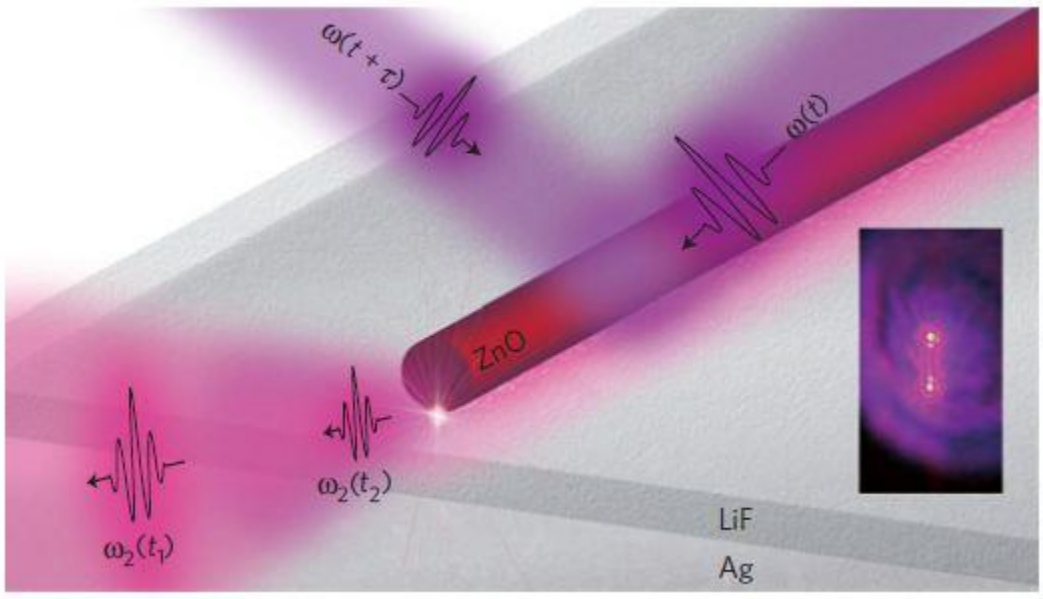

Figure 5.12: Physical Structure of the Ag-LiF-ZnO Nanowire ultrafast room temperature plasmon laser.

5.2.1 Simulation Setup of Ag-LiF-ZnO Nanowire Structure

The silver and LiF layers are place on Si with 100 nm and 10 nm thickness respectively (shown in Fig. 5.13). Corresponding materials were modeled with sampled data. A cylindrical structure of 150 nm is placed on the LiF layer to create the ZnO nanowire. The ZnO gain medium was modelled with 'four level two electron' model with parameters: the wavelength of pumping 355 nm, emission wavelength of 385 nm, μ_{21}= τ-

$_{30}$ = 350 ps [5], $\tau_{32}=\tau_{10}$=1 ps and population density of ZnO at room temperature is used. ZnO with sampled data was used as the base material four level two electron gain medium to accurately model the dispersion relation. Two Gaussian sources with thin fill lens and time delay between them are used to simulate the source. The boundary condition of the simulation region and calculation of emission spectrum were done similarly as the CdS MIS structure. The result of the simulation is given below.

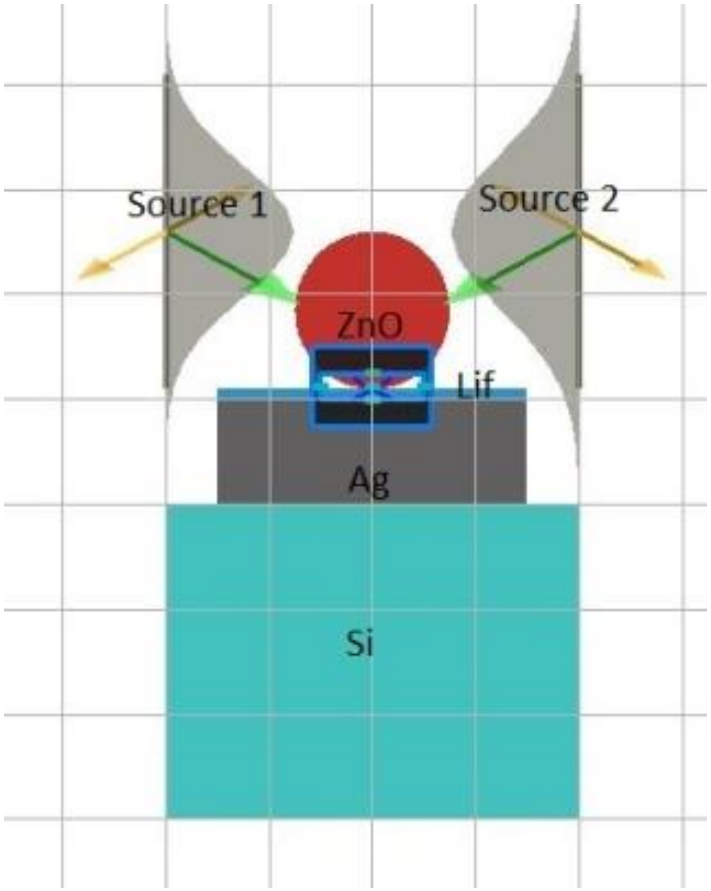

Figure 5.13: Simulation setup of the Ag-LiF-ZnO room temperature plasmon laser.

5.2.2 Lasing Action in Ag-LiF-ZnO Nanowire

In Fig. 5.14 the emission spectrum of TM mode (blue) and TE mode (red) of the system is given. From the plot, it is evident that the peak emission occurs at 387 nm.

Because the surface plasmon frequencies of silver-air ($\hbar\omega_{sp}$=3.65 eV) and silver-ZnO ($\hbar\omega_{sp}$=2.9 eV) encompasses the exciton energies E=3.2 eV. The experimental emission occurs at 385 nm which is slightly less than simulated result. This can be explained by the energy redistribution between excitons of different energy states at room temperature.

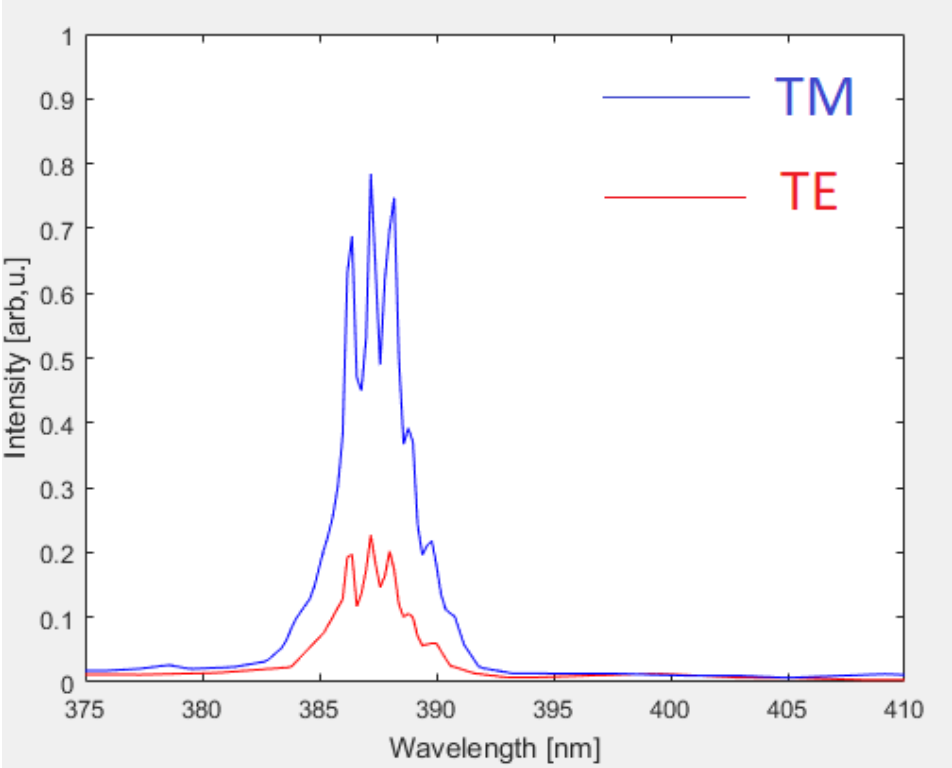

Figure 5.14: Laser emission spectra of TM and TE mode of the Ag-LiF-ZnO nanowire MIS structure.

5.3 Summary

The results obtained from the simulation matches to the experimental data with great degree of accuracy. Thus our simulation also confirm the room temperature operation the proposed above mentioned laser structures.

CHAPTER 6

Conclusion and Future Works

Plasmonic lasers can greatly contribute to integrating the photonic and electronic circuit by reducing the size of the laser to match the electronic circuit components' nanoscale size. But a huge obstacle towards this implementation is their operational requirement of cryogenic temperature. High electron scattering and radiation loss are main hurdle towards their room temperature operation. In this work we simulated two experimental works of room temperature plasmonic laser which shows both low threshold and room temperature operation [5,6]. Both structures opt for Ag metal which is known for its comparatively lower imaginary part of permittivity and more negative real part of permittivity which cause simultaneously low metallic loss and higher plasmonic confinement. They both employ metal-insulator-semiconductor hybrid structure to include a dielectric spacer layer between the metal and the gain medium to increase the confinement in the cavity to overcome the metal loss. Moderate Q factor with nanoscale mode volume is needed to obtain lasing action at room temperature. The first laser proposed by Ma et al [5], increases Q factor of the cavity by employing total internal reflection in the cavity and second laser proposed by Sidiropoulos [6] increases Q factor by matching the surface plasmon frequency and the emission frequency of the ZnO excitons. Our simulations also confirm their room temperature operation. In our

simulation room temperature environment was modeled by using all the material refractive index and permittivity data of room temperature. Data required for modeling the gain medium i.e. the electron population density data were also used of room temperature to correctly model the room temperature conditions. Besides, room temperature operation of plasmonic laser there are a number of area to be addressed for practical plasmonic laser implementation. Those areas with opportunities for future works and developments are presented below.

6.1 Future Works

- Until now most of the demonstrated plasmonic lasers are optical pump based. For the purpose of integration of the photonic circuit with electronic circuit option for electron injection pumping is necessary. Thus optical pumping poses a major obstacle in this regard for requiring another light source to pump the laser. More future work is possible in this regard.
- Another issue for application of plasmonic laser is the divergence of emission. In many applications, spatial coherence is necessary for proper operation of the device. More development of plasmonic laser in emitting spatially coherent beam is also possible.
- For metal-inductor-semiconductor hybrid structure improvement other few combinations have been proven to be useful. i.e. Al metal can be used instead of Ag for better commercial value and integrity of the MIS structure.

REFERENCES

[1] T.H. Maiman, Nature187, 493–494(1960).

[2] NIF's future ignites with 192-beam shot, LLNL community news, https://newsline.llnl.gov/ rev02/articles/2009/mar/03. 06.09-nif.php, date of last visit: 18 February 2012.

[3] NIF breaks megaJoule barrier, LLNL community news, https://newsline.llnl.gov/ rev02/articles/2009/mar/03.13. 09-nif.php, date of last visit: 18 February 2012.

[4] E. Murphy, Nat. Photonics4, 287(2010).

[5] R. M. Ma, R. F. Oulton, V. J. Sorger, G. Bartal and X. Zhang, "Room-temperature sub-diffraction-limited plasmon laser by total internal reflection," NATURE MATERIALS, vol. 10, Feb. 2011.

[6] T. P. H. Sidiropoulos, R. Röder, S. Geburt, O. Hess, S. A. Maier, C. Ronning and R. F. Oulton, "Ultrafast plasmonic nanowire lasers near the surface plasmon frequency,"NATURE PHYSICS, ADVANCE ONLINE PUBLICATION, Sep. 2014.

[7] N. Ledentsov, "Quantum dot laser," Semiconductor Science and Technology, vol. 26, no. 1, p. 014001, 2010.

[8] A. N. Oraevsky, M. Scully, and V. L. Velichansky, "Quantum dot laser," Quantum electronics, vol. 28, no. 3, pp. 203–208, 1998.

[9] C.-Z. Ning, "Semiconductor nanolasers," Physica Status Solidi (b), vol. 247, no. 4, pp. 774–788, 2010.

[10] M. T. Hill, M. Marell,E. S. P. Leong, B. Smalbrugge, Y. Zhu, M. Sun, P. J. V. Veldhoven, E. J. Geluk, F. Karouta, Y. S. Oei, R. *Ẅ*otzel, C.-Z. Ning, and M.K. Smit, Opt. Express 17, 11107–11112 (2009).

[11] M.A. Noginov, G. Zhu, A.M. Belgrave, R. Bakker, V.M. Shalaev, E.E. Narimanov, S. Stout, E. Herz, T. Suteewong, and U. Wiesner, Nature460, 1110–1113 (2009).

[12] R.F. Oulton, V.J. Sorger, T. Zentgraf, R.M. Ma, C. Gladden, L. Dai, G. Bartal, and X. Zhang, Nature 461, 629–632 (2009).

[13] S.-H. Kwon, J.-H. Kang, C. Seassal, S.-K. Kim, P. Regreny, Y.-H. Lee, C.M. Lieber, and H.-G. Park Nano, Lett. 10, 3679–3683 (2010).

[14] R. M. Ma, R. F. Oulton, V. J. Sorger, G. Bartal, and X. Zhang, Nat. Mater.10, 110–113 (2011).
[15] R. A. Flynn, C. S. Kim, I. Vurgaftman, M. Kim, J. R. Meyer, A. J. M¨akinen, K. Bussmann, L. Cheng, F.-S. Choa, and J.P. Long, Opt. Express19, 8954 (2011).
[16] M.J.H. Marell, B. Smalbrugge, E.J. Geluk, P.J.V. Veldhoven, B. Barcones, B. Koopmans, R. N¨otzel, M.K. Smit, and M.T. Hill, Opt. Express19, 15109–15118(2011).
[17] A.M. Lakhani, M.-K. Kim, E.K. Lau, and M.C. Wu, Opt. Express19, 18237–18245 (2011).
[18] C.-Y. Wu, C.-T. Kuo, C.-Y. Wang, C.-L. He, M.-H. Lin, H. Ahn, and S. Gwo, Nano Lett., dx.doi.org/10.1021/ nl2022477 (2011).
[19] M.I. Stockman, J. Opt. 024004 (2010).
[20] T. Liebermann and W. Knoll, Coll. Surf. 171, 115–130 (2000).
[21] P. Anger, P. Bharadwaj, and L. Novotny, Phys. Rev. Lett. 96, 113002 (2006).
[22] A. Kinkhabwala, Z. Yu, S. Fan, Y. Avlasevich, K. M¨ullen, and W.E. Moerner, Nat. Photonics3, 654–657 (2009).
[23] D. Genov, R. Oulton, G. Bartal, and X. Zhang, Phys. Rev. B83, 245312 (2011).
[24] W. Srituravanich, L. Pan, Y. Wang, C. Sun, D.B. Bogy, and X. Zhang, Nat. Nanotechnol.3, 733–737 (2008).
[25] Y. Kim, S. Kim, H. Jung, E. Lee, and J.W. Hahn, Opt. Express17, 19476–19485 (2009).
[26] Z. Xie, W. Yu, T. Wang, H. Zhang, Y. Fu, H. Liu, F. Li, Z. Lu, and Q. Sun, Plasmonics6, 565–580 (2011).
[27] D.J. Bergman and M.I. Stockman, Phys. Rev. Lett. 90, 027402 (2003).
[28] J. Seidel, S. Grafstrom, and L. Eng, Phys. Rev. Lett. 94, 177401 (2005).
[29] M. Ambati, S.H. Nam, E. Ulin-Avila, D.A. Genov, G. Bartal, and X. Zhang, Nano Lett.8, 3998 (2008).
[30] G. Plotz, H. Simon, and J. Tucciarone, “Enhanced total reflection with surface plasmons,” JOSA, vol. 69, no. 3, pp. 419–422, 1979.
[31] A. Sudarkin and P. Demkovich, “Excitation of surface electromagnetic waves on the boundary of a metal with an amplifying medium,” Sov. Phys. Tech. Phys, vol. 34, no. 764766, p. 57, 1989.
[32] J. Seidel, S Grafstr*ö*m, and L Eng, “Stimulated emission of surface plasmons at the interface between a silver film and an optically pumped dye solution,” Physical Review Letters, vol. 94, no. 17, p. 177401, 2005.

[33] M. Noginov, V. A. Podolskiy, G Zhu, M Mayy, M Bahoura, J. Adegoke, B. Ritzo, and K Reynolds, “Compensation of loss in propagating surface Plasmon polariton by gain in adjacent dielectric medium,” Optics Express, vol. 16, no. 2, pp. 1385–1392, 2008.

[34] F. van Beijnum, P. J. van Veldhoven, E. J. Geluk, M. J. de Dood, W Gert, and M. P. van Exter, “Surface plasmon lasing observed in metal hole arrays,” Physical Review Letters, vol. 110, no. 20, p. 206802, 2013.

[35] F. van Beijnum, P. J. van Veldhoven, E. J. Geluk, G. W’t Hooft, and M. P. van Exter, “Loss compensation of extraordinary optical transmission,” Applied Physics Letters, vol. 104, no. 6, p. 061112, 2014.

[36] X. Meng, J. Liu, A. V. Kildishev, and V. M. Shalaev, “Highly directional spaser array for the red wavelength region,” Laser & Photonics Reviews, vol. 8, no. 6, pp. 896–903, 2014.

[37] W. Zhou, M. Dridi, J. Y. Suh, C. H. Kim, D. T. Co, M. R. Wasielewski, G. C. Schatz, T. W. Odom, et al., “Lasing action in strongly coupled plasmonic nanocavity arrays,” Nature Nanotechnology, vol. 8, no. 7, pp. 506–511, 2013.

[38] J. Y. Suh, C. H. Kim, W. Zhou, M. D. Huntington, D. T. Co, M. R. Wasielewski, and T. W. Odom, “Plasmonic bowtie nanolaser arrays,” Nano Letters, vol. 12, no. 11, pp. 5769–5774, 2012.

[39] H.-Y. Wu, L. Liu, M. Lu, and B. T. Cunningham, “Lasing emission from plasmonic nanodome arrays,” Advanced Optical Materials, vol. 4, no. 5, pp. 708–714, 2016.

[40] M. J. H. Marell, B. Smalbrugge, E. J. Geluk, P. J. V. Veldhoven, B. Barcones, B. Koopmans, R. Nötzel, M. K. Smit, and M. T. Hill, "Plasmonic distributed feedback laser at telecommunication wavelegths", Opt. express, vol. 19, pp. 15109- 15118, 2011.

[41] S. H. Kwon, J. H. Kang, C. Seassal, S. K. Kim, P. Regrency, Y. H. Lee, C. M. Lieber, H. G. Park, "Subwavelength plasmonic lasing from a semiconductor nanodisk with silver nanopan cavity", Nano Letters, vol. 10, pp. 3679-3683, 2009.

[42] Kashiwa, T., Yoshida, N. and Fukai, I. (1990) ,“A treatment by the Finite-Difference Time-Domain Method of the Dispersive Characteristics Associated with Orientation Polarization,” IEEE Transactions on Antennas and Propagation, E73, 1326-1328.

[43] S. A. Maier, ‘’Plasmonics: Fundamentals and Applications’’, Springer, New York, 2007.

[44] W. L. Barnes, A. Dereux, and T. W. Ebberson, "Surface plasmon subwavelength optics" Nature, VOL 424,Aug. 2003.

[45] P. B. Johnson and R. W. Christy, "**Optical Constants of the Noble Metals",** Phys. Rev. B **6**, 4370 (1972) – Published 15 December 1972

[46] K. A. Willets and R. P. Van Duyne, "Localized surface plasmon resonance spectroscopy and sensing," Annu. Rev. Phys. Chem. 58, 267 (2007).

[47] S. Lal, S. Link, and N. J. Halas, "Nano-optics from sensing to waveguiding," Nature Photonics, vol. 1, no. 11, pp. 641–648, 2007.

[48] P. Andrew and W. Barnes, "Energy transfer across a metal film mediated by surface plasmon polaritons," Science, vol. 306, no. 5698, pp. 1002–1005, 2004.

[49] P. Anger, P. Bharadwaj, and L. Novotny, "Enhancement and quenching of single-molecule fluorescence," Physical Review Letters, vol. 96, no. 11, p. 113002, 2006.

[50] Bouhelier and G. P. Wiederrecht, "Surface plasmon rainbow jets," Opt. Lett. 30, 884-886 (2005).

[51] P. W. Carlin, "The minimum spot size for a focused layer and the uncertainty relation," Proc. IEEE 52, 1371 (1964).

[52] E. H. K. Stelzer and S. Grill, "The uncertainty principle applied to estimate focal spot dimensions," Opt. Commun. 173, 51 (2000).

[53] E. H. K. Stelzer, "Light microscopy - beyond the diffraction limit?" Nature 417, 806 (2002).

[54] M. Born and E. Wolf, Principles of optics : electromagnetic theory of propagation, interference and diffraction of light (Cambridge University Press, Cambridge; New York, 1999), 7th ed.

[55] L. Novotny and B. Hecht, Principles of nano-optics (Cambridge University Press, Cambridge, 2012), 2nd ed.

[56] Purcell Effect - Wikipedia, [Online], Available: https://en.wikipedia.org/wiki/Purcell_effect

[57] E. Purcell, "Spontaneous emission probabilities at radio frequencies", Phys. Rev. 69, 681 (1946).

[58] E. Yablonovitch ,"Inhibited Spontaneous Emission in Solid-State Physics and Electronic", Physical Review Letters 58, 2059 (1987).

[59] K. J. Vahala „Optical Microcavities" Nature 424, 839-846 (2003).

[60] R. F. Oulton, V. J. Sorger, D. F. P. Pile, D. A. Genov and X. Zhang "A hybrid plasmonic waveguide for subwavelength confinement and long-range propagation", Nature Photonics 2, 496-500 (2008).

[61] R.-M. Ma, R. F. Oulton, V. J. Sorger, G. Bartal and X. Zhang Nature Materials 10, 110-113 (2010).

[62] V. J. Sorger, R. F. Oulton, J. Yao, G. Bartal and X. Xiang, Nano Lett. 9, 3489-3493 (2009).
[63] V. J. Sorger et al. In review at Physical Review Letters (2011).
[64] J. Shainline, G. Fernandes, Z. Liu and J. Xu, Frontiers in Optics, FWZ4 San Jose (2009).
[65] K. J. Vahala „Optical Microcavities" Nature 424, 839-846 (2003).
[66] Purcell, E. Spontaneous emission probabilities at radio frequencies. Phys. Rev. 69, 681 (1946).
[67] Miyazaki, H & Kurokawa, Y. Squeezing Visible Light Waves into a 3-nm-Thick and 55-nmLong Plasmon Cavity. Phys. Rev. Lett. 96, 097401 (2006).
[68] Weeber, J.-C., Bouhelier, A., Colas de Francs, G., Markey, L. & Dereux, A. Submicrometer In-Plane Integrated Surface Plasmon Cavities. Nano Lett. 7, 1352-1359 (2007).
[69] Min, B., Ostby, E., Sorger, V.J., Ulin-Avila, E.,, Yang, L., Zhang, X. & Vahala, K. High-Q surface-plasmon-polariton whispering-gallery microcavity. Nature 457, 455 - 458 (2009).
[70] V. J. Sorger, R. F. Oulton, J. Yao, G. Bartal and X. Xiang, Nano Lett. 9, 3489-3493 (2009).
[71] Bergman, D. J. & Stockman, M. I. Phys. Rev. Lett. 90, 027402 (2003).
[72] V. J. Sorger et al. Unpublished work (2011).
[73] M. Hill. et al. Optics Express 17, 11107-11112 (2009).
[74] M. P. Nezhad et al. Nature Photonics 4, 395-399 (2010).
[75] K. Yu, A. Lakhani and M. Wu Optics Express 18, 8790–8799 (2010).
[76] S.-H. Kwon, J.-H. Kang, C. Seassal, S.-K. Kim, P. Regreny, Y.-H. Lee, Ch. M. Lieber and H.-G. Park Nano Letters 10, 9, 3679–3683 (2010).
[77] M. A. Noginov et al. Nature 460, 1110-1113 (2009).
[78] Notice, the convention used here defers from the TM wave definition with respect to the dielectric-air interface where the total internal reflection takes place
[79] Poon, A. W., Courvoisier, F. & Chang, R. K. Multimode resonances in square-shaped optical microcavities. Optics Letters 26, 632-634 (2001)
[80] K. S. Yee et al., "Numerical solution of initial boundary value problems involving maxwells equations in isotropic media," IEEE Trans. Antennas Propag, vol. 14, no. 3, pp. 302–307, 1966.
[81] A. Taflove, S. C. Hagness, et al., "Computational electrodynamics: The finite difference time-domain method," Norwood, 2nd Edition, MA: Artech House, l995, 1995.

[82] K. S. Kunz and R. J. Luebbers, The finite difference time domain method for electromagnetics. CRC press, 1993.

[83] J. A. Roden and S. D. Gedney, “Efficient implementation of the uniaxial-based PML media in three-dimensional nonorthogonal coordinates with the use of the fdtd technique,” Microwave and Optical Technology Letters, vol. 14, no. 2, pp. 71–75, 1997.

[84] C. M. Rappaport, “Perfectly matched absorbing boundary conditions based on anisotropic lossy mapping of space,” IEEE Microwave and Guided Wave Letters, vol. 5, no. 3, pp. 90–92, 1995.

[85] S.-H. Chang and A. Taflove, “Finite-difference time-domain model of lasing action in a four-level two-electron atomic system,” Optics Express, vol. 12, no. 16, pp. 3827–3833, 2004.

[86] Refractive index of CdS (Cadmium sulfide)- Treharne. [Online], Available: https://refractiveindex.info/?shelf=main&book=CdS&page=Treharne

[87] R. M. Ma, R. F. Oulton, V. J. Sorger, G. Bartal and X. Zhang," Supplementary Information" on "Room-temperature sub-diffraction-limited plasmon laser by total internal reflection," NATURE MATERIALS, vol. 10, Feb. 2011

[88] A. V. Akimov et al, "Generation of single optical plasmons in metallic nanowires coupled to quantam dots," Nature, vol. 5, pp. 470-474, 2009.

[89] J. Wiersig, "Formation of long lived, scarlike modes near avoided resonance crossings in optical microcavities," Phys. Rev. Letter, vol. 97, pp. 253901, 2006.

[90] B. Liu, R. Chen, X. L. Xu, D. H. Li, Y. Y. Zhao, Z. X. Shen, Q. H. Xiong, H. D. Sun,"Exciton related photoluminescence and lasing in CdS nanobelts," Journal of physical chemistry, vol. 115, pp. 12826-12830, 2011.

[91] J. W. Goodman,Introduction to Fourier optics (Roberts & Co., Englewood, Colo., 2005), 3rd ed.